Marine Geology 475 (2024) 107361

Contents lists available at ScienceDirect

Marine Geology

journal homepage: www.elsevier.com/locate/margo

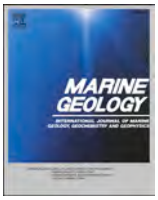

Dismantling of an isolated tropical carbonate platform through flank collapse and canyon erosion, Coral Sea, Northeast Australia

Christian Betzler [a,*], Sebastian Lindhorst [a], Carola Hincke [a], Jan Oliver Eisermann [a], Or M. Bialik [b], Alex Petrovic [c], Jesus Reolid [d], Robin J. Beaman [e], Jody M. Webster [f], Thomas Lüdmann [a], Christian Hübscher [g]

[a] Institut für Geologie, Universität Hamburg, Bundesstr. 55, 2046 Hamburg, Germany
[b] Institut für Geologie und Paläontologie, Erdsystemforschung, Corrensstr. 24, 48149 Münster, Germany
[c] Rue du Château 13A, 5300 Seilles, Belgium
[d] Departamento de Estratigrafía y Paleontología, Universidad de Granada, Avenida Fuentenueva s/n, 18071, Granada, Spain
[e] College of Science and Engineering, James Cook University, Cairns 4870, Queensland, Australia
[f] Geocoastal Research Group, School of Geosciences, University of Sydney, Madsen Building (F09), Sydney 2006, NSW, Australia
[g] Institut für Geophysik, Universität Hamburg, Bundesstr. 55, 2046 Hamburg, Germany

ARTICLE INFO

Editor Name: Michele Rebesco

Keywords:
Mesophotic carbonate platform
Mass Transport complex
Calciturbidite
Slope instability
Submarine rockfall

ABSTRACT

The steep slopes of carbonate platforms frequently display large-scale sediment destabilization features like rockfalls, mass transport complexes, and slope erosion. The processes and factors triggering such instabilities and how they interact are a matter of ongoing discussion. We use hydroacoustic, sedimentological, and seafloor imaging data to map and characterize slope instabilities and potential controlling factors at the flank of the isolated Tregrosse carbonate bank in the Coral Sea, northeast Australia. Erosion of gullies and submarine valleys is concentrated in slope segments with the platform rim at several 10s of meters of water depth, i.e. where there is potential for sediment transfer from the bank interior to the slope. Gravity core data indicate that most sediment export from the platform occurs during sea-level fall. The toe of slopes neighboring segments with a shallower platform rim are mostly characterized by mass-transport complexes of platform rim and upper slope rocks forming extended block fields. Distal slope areas are dismantled through submarine landslides resulting in scalloped head scarps. The basal detachment surface of these submarine landslides appears to be rooted in several 100 s of meters in the subsurface at a lithological heterogeneity, which is documented by a gamma-ray peak in the downhole logging data from Ocean Drilling Program Site 817. Our findings show that (1) canyon erosion, (2) platform rim and upper slope destabilization as well as (3) lower slope dismantling, largely act independently of each other to destabilize the flanks of the carbonate bank. The complexity of the carbonate platform dismantling processes and the corresponding controlling factors shown in this study should also be considered when interpreting seismic morphological data.

1. Introduction

The gravitational slope depositional processes at carbonate platform margins have been the focus of several studies discussing the differences between carbonate and siliciclastic depositional systems. One emphasis was on the export of loose sediment generated in the neritic realm through suspensions in the form of nepheloid layers (Wilson and Roberts, 1995) and sediment gravity flows (Andresen et al., 2003; Droxler and Schlager, 1985; Glaser and Droxler, 1993; Jorry et al., 2008, 2010, 2020; Schlager et al., 1994; Mulder et al., 2012, 2014; Webster et al., 2012; Wunsch et al., 2017; Counts et al., 2021).

Another focus was on carbonate platform margin collapses and mass transport complexes (MTCs) that are known from several recent carbonate platforms. Along the slope of the Great and Little Bahama Bank (Atlantic Ocean), these MTC systems are located at the upper bank margin (Mullins and Hine, 1989; Jo et al., 2015) and the middle to lower slope (Mulder et al., 2012; Principaud et al., 2015; Tournadour et al., 2015). This is also the case for the Lansdowne Bank (southwest Pacific

* Corresponding author
E-mail address: christian.betzler@uni-hamburg.de (C. Betzler).

https://doi.org/10.1016/j.margeo.2024.107361
Received 18 April 2024; Received in revised form 7 July 2024; Accepted 7 July 2024
Available online 14 July 2024

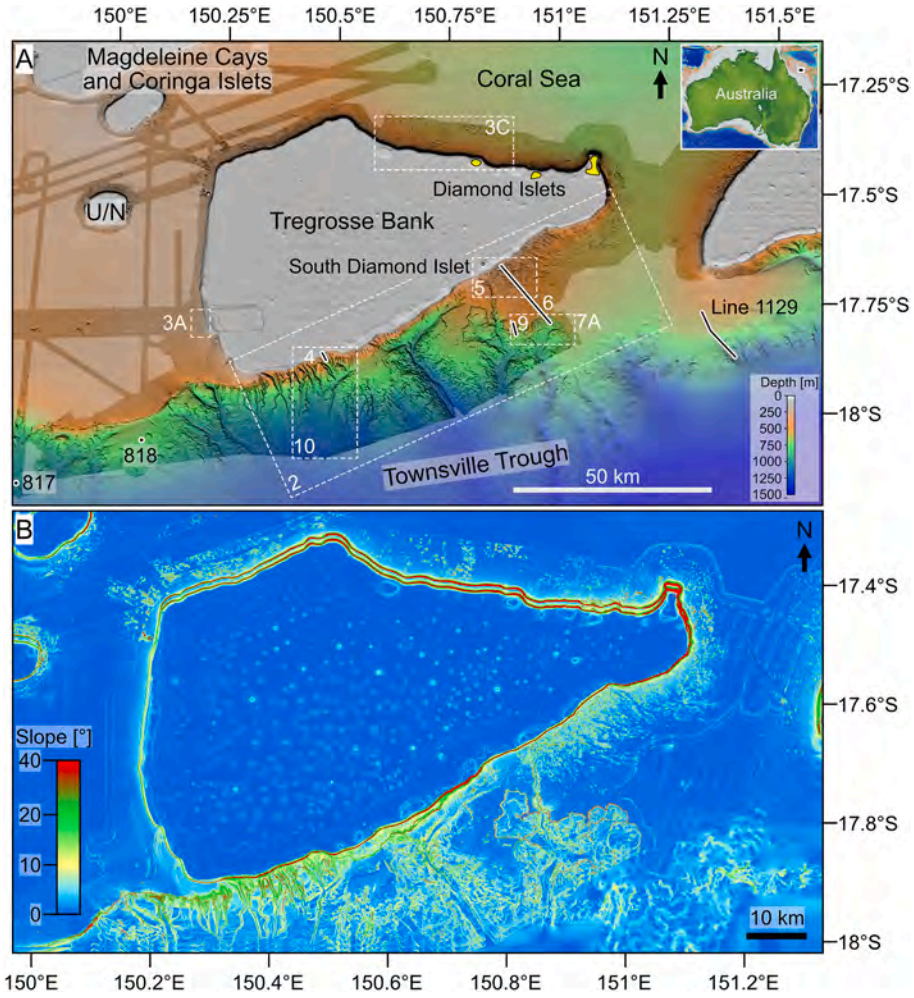

Fig. 1. **A:** Location and map of Tregrosse Bank. Map uses multibeam data from RV *Sonne* Cruise SO292 merged with data from the RV *Falkor* cruises FK200429 and FK200802 (Siwabessy and Spinoccia, 2022) and Australian gbr100 data (Beaman, 2010) as background. Line 1129 indicates the position of the part of the Shell seismic line 1129 shown in Fig. 7. White numbers, stippled rectangles, and white lines refer to details shown in the corresponding figs. U/N: unnamed carbonate bank; yellow areas: islands; 817, 818: ODP sites. **B:** Map of slope inclinations of the flanks of Tregrosse Bank. Note that the steepest slopes are located to the south, southeast, and the north of the bank. The colour code used for slope inclination values is not linear to allow for better visualization of the occurrence of steeply inclined slope parts. (For interpretation of the references to colour in this figure legend, the reader is referred to the web version of this article.)

Ocean), where bank edges and submarine slope failures were described (Etienne et al., 2021), and the land-attached Al Wajh platform in the Red Sea that is currently in a state of disintegration (Petrovic et al., 2023). Gravitational collapse of the carbonate platform shelf edge (Webster et al., 2016) and upper slope (Puga-Bernabéu et al., 2017) was also described from the Great Barrier Reef province and from carbonate platforms in the Mozambique Channel (Counts et al., 2018).

From the fossil record, the Cretaceous to Eocene carbonate slopes of the Apulian carbonate platform cropping out in the Gargano Promontory (Italy) and in Albania provide well-studied examples of MTCs along slopes (Bosellini et al., 1993; Borgomano, 2000; Morsilli et al., 2002; Eberli et al., 2005; Le Goff et al., 2020; Morsilli et al., 2021). Distinct sources for these MTCs were reconstructed by assessing the diagenesis of the reworked deposits (Sælen et al., 2024), which indicates that such debris are sourced from the shallow platform part affected by meteoric diagenesis and from upper slope deposits affected by marine burial diagenesis. Lehrmann et al. (2020) relate large-scale Triassic carbonate platform margin failures in China to a high margin elevation with a lack of buttressing by basin-filling deposits.

Different trigger mechanisms for slope and margin destabilization have been discussed in previous studies. Besides broader-scale geodynamic influences, processes evoked are gravitational collapse through sediment overloading due to the vertical growth of the reef wall (Ginsburg et al., 1991), oversteepening of the slope (Adams and Kenter, 2014), differential compaction of distal slope and basinal deposits (Frost and Kerans, 2009; Nooitgedacht et al., 2018a), porewater overpressure of confined sub-seafloor aquifers (Spence and Tucker, 1997), fluid seepage (Micallef et al., 2021), and mechanical weaknesses at the boundaries of lithological cycles (Puga-Bernabéu et al., 2022). Numerical modeling of the Great Bahama Bank slope failures and submarine landslides indicates that porewater overpressure is a transient feature achieved during platform emersion, i.e. sea-level lowstands, and that the horizontal stress distribution counteracts the effect of overpressure build-up in the lower platform slope (Busson et al., 2021). A similar context was also discussed for Ediacarian carbonate platforms in China (Liu et al., 2022).

For the Bahamas, Great Barrier Reef, and Lansdowne Bank discussion has focused on how bank margin collapses and slope failures are associated with erosional features such as submarine channels and canyons (Puga-Bernabéu et al., 2011; Mulder et al., 2012; Wunsch et al., 2017; Tournadour et al., 2017; Etienne et al., 2021). In these instances, retrograding erosion has been evoked as the dominant process to explain MTC emplacement and initiate up-slope lengthening of incised submarine valleys or canyons.

Despite these multiple studies there still is limited understanding of the interrelation of the different slope disintegration processes such as

submarine landslides, submarine rockfalls, and slope erosion. This is especially true for mesophotic carbonate platforms: Such platforms are characterized by carbonate factories lying at water depths of several tens of meters, where only little sediment may be exported to the platform's steeper flanks and the adjacent basins (Bialik et al., 2024). In this context, the slopes of the isolated Tregrosse carbonate platform on the Queensland Plateau in the Coral Sea were identified as ideal to help decipher how these processes interact. The slopes and adjacent basin of the bank were mapped, sampled, and visually analyzed with data collected during RV *Sonne* Cruise SO292. We present a series of slope destabilization features and discuss their interrelation for the disintegration of an isolated tropical carbonate platform. Results may serve as a modern counterpart to assist the interpretation of carbonate platform dismantling within the geological record.

2. Geological setting

The East Australian carbonate province, which encompasses the Great Barrier Reef, the Marion Plateau, and the Queensland Plateau, has been the focus of integrated sedimentological, stratigraphic, and paleoceanographic research during Ocean Drilling Program (ODP) Leg 133 which cored several sites as far down as the basement (Davies et al., 1991). The Queensland Plateau hosts several large, isolated carbonate banks ~100 km long and tens of km wide. This study focuses on Tregrosse Bank, which is a mesophotic carbonate platform (Orme, 1977; Reolid et al., 2024) with minor sand cays (Diamond Islets and South Diamond Islet), and shallow-water reefs mostly located in its eastern part (Fig. 1A). The shallowest part of Tregrosse Bank (< 100 m water depth) is approximately 100 km long by 50 km wide. Today, large parts of the bank interior are occupied by *Halimeda* meadows and bioherms (mounds) in water depths of 50 to 65 m (Reolid et al., 2024).

The plan shape of the bank is nearly triangular (Fig. 1). It is situated in the path of the South Equatorial Current (SEC) which diverts around the isolated banks of the Queensland Plateau (Ceccarelli et al., 2013). The flow branch impinging on the eastern and southern bank edges and slopes is the North Caledonia Jet (Ganachaud et al., 2007; Kessler and Cravatte, 2013). The southern flank of Tregrosse Bank which faces the Townsville Trough basin is exposed to a westerly-directed surface current flowing along the platform flank at 0.4–0.8 m s^{-1} with models indicating that this flow direction reaches down to a water depth of at least 103 m, albeit with lower velocity (ereefs.aims.gov.au). The northern flank of Tregrosse Bank is generally ocean-current protected. However, currents of tidal origin (i.e. the reverse of this dominant current) and slightly accelerated (0.2–0.4 m s^{-1}) are observed in the passage between Magdaleine Cays/Coringa Islets and Tregrosse Bank (ereefs.aims.gov.au).

The wind regime around the Queensland Plateau shows a strong seasonality, dominated by the trade winds. Tregrosse Bank is therefore lying in the path of a predominately southeast-to-northwest wind regime. The Queensland Plateau is affected by westward-moving tropical cyclones, with storm tracks clustering over the study area (Reolid et al., 2024; Knapp et al., 2010).

The ca. 100 km wide southern flank of the bank is oriented towards the southeast, i.e. it is the up-current side of the bank. The west-facing, down-current flank of the bank is 57 km wide, and the northern irregular flank is 97 km wide. The water depth in the inner bank is between 70 and 50 m, with shallower areas lying in its eastern reaches. The bank has a margin located at a water depth of around 60 m in its western part and several sand cays (Diamond Islets) characterize the eastern and southeastern parts (Figs. 1A, B).

Tregrosse Bank is a remnant of a larger bank that partially drowned during the late Middle Miocene (Mutter, 1977; Davies et al., 1989; Betzler et al., 2024). The edge of this drowned edifice has been identified in several seismic lines (Davies et al., 1989, 1991; Betzler et al., 2024) and is now lying at a water depth of 450 m to 500 m. Geomorphologically it is expressed as a terrace, such as north of ODP sites 817 and 818 (Fig. 1A).

3. Methods

Bathymetric data were acquired at a cruising speed of 5.5 to 8 kn using the Kongsberg EM122 (12 kHz) multibeam system of RV *Sonne*. Sound-velocity and salinity profiles of the water column were obtained from conductivity-temperature-depth (CTD) probe measurements and by using XSV-02 probes (Lockheed Martin, Sippican Inc.). Data processing using Qimera software (v2.4.8, QPS) comprised manual cleaning and surface generation with cell sizes of 20 and 30 m. Bathymetric data were corrected for astronomic tides using tidal predictions from AusTides software (Australian Hydrographic Office; stations 57,845 Magdelaine Cays and 57,850 Willis Islet). Data collected by RV *Sonne* cruise SO292 were supplemented by Kongsberg EM302 multibeam data collected during RV *Falkor* cruises FK200429 and FK200802 (Siwabessy and Spinoccia, 2022). Visualization and analyses were done using GlobalMapper (Blue Marble Geographics).

Sub-bottom profiles were recorded using the parametric sediment echosounder Atlas Parasound PS70 (mk2) of RV *Sonne* with the software Parastore (Teledyne RESON GmbH). The desired primary high frequency was 18 kHz, and the secondary low frequency was 4 kHz. The depth of seafloor penetration reaches 80 to >140 m. Data were converted to SEG-Y formatwith the tool ps32segy (Hanno Keil, University of Bremen, Germany) and processed using the software ReflexW (v9.5, Sandmeier Software). Time-depth conversion of Parasound data was done with a sound velocity of 1500 ms^{-1}.

Ocean-floor video and still images were acquired with an OFOS (Ocean Floor Observation System), a passively-towed sled equipped with two cameras (Canon EOS R5 and Marshal CV350-5 × 2.3 video camera) and four LED lights (Sealite Sphere 5150). For scale, three laser pointers projected an equidistant (40 cm) triangle of points into the field of view. Overlapping still images at various sites were stitched into panoramas using Affinity Photo (v2.1, Serif). Photogrammetry of images

Table 1
Radiocarbon ages for cores SO292_034GC and SO292_090GC. For details on analyses see the methods section.

Lab ID	Sample ID	Sample			Conv. age (yrs BP)		Isotopes (o/oo)		Calibrated (ka BP)			
		Depth (m)	Material	Amount (mg)	Age	Error	$\delta^{13}C$	$\delta^{18}O$	Range (sigma 2)		Median	Error
Beta-688,172	SO292_034-2GC_005	0.02	Mixed planct. Foramniferas	25.3	1040	30	+2.3	−1.0	0.34	0.61	0.48	0.14
Beta-663,815	SO292_034-2GC_030	0.27	Mixed planct. Foramniferas	10.0	4280	30	+1.1	−1.5	4.04	4.39	4.21	0.18
Beta-663,816	SO292_034-2GC_050	0.47	Mixed planct. Foramniferas	12.3	8790	30	+0.8	−1.5	9.12	9.44	9.29	0.16
Beta-663,817	SO292_034-2GC_110	1.07	Mixed planct. Foramniferas	14.4	23,420	90	+1.0	0.0	26.47	27.11	26.84	0.32
Beta-688,173	SO292_090-1GC_010	0.10	Mixed planct. Foramniferas	10.7	1470	30	+2.0	−1.2	0.71	980	0.85	0.14
Beta-685,510	SO292_090-1GC_040	0.40	Mixed planct. Foramniferas	9.6	2990	30	+2.0	−2.2	2.43	2.74	2.60	0.16
Beta-685,511	SO292_090-1GC_100	1.00	Mixed planct. Foramniferas	15.8	6460	30	+2.2	−1.8	6.56	6.89	9.73	0.17
Beta-676,506	SO292_090-1GC_140	1.40	Mixed planct. Foramniferas	11.4	9650	30	+0.4	−1.8	10.22	10.54	10.47	0.16
Beta-676,507	SO292_090-1GC_170	1.70	Mixed planct. Foramniferas	16.3	12,570	40	+1.2	−1.0	13.78	14.19	13.99	0.21

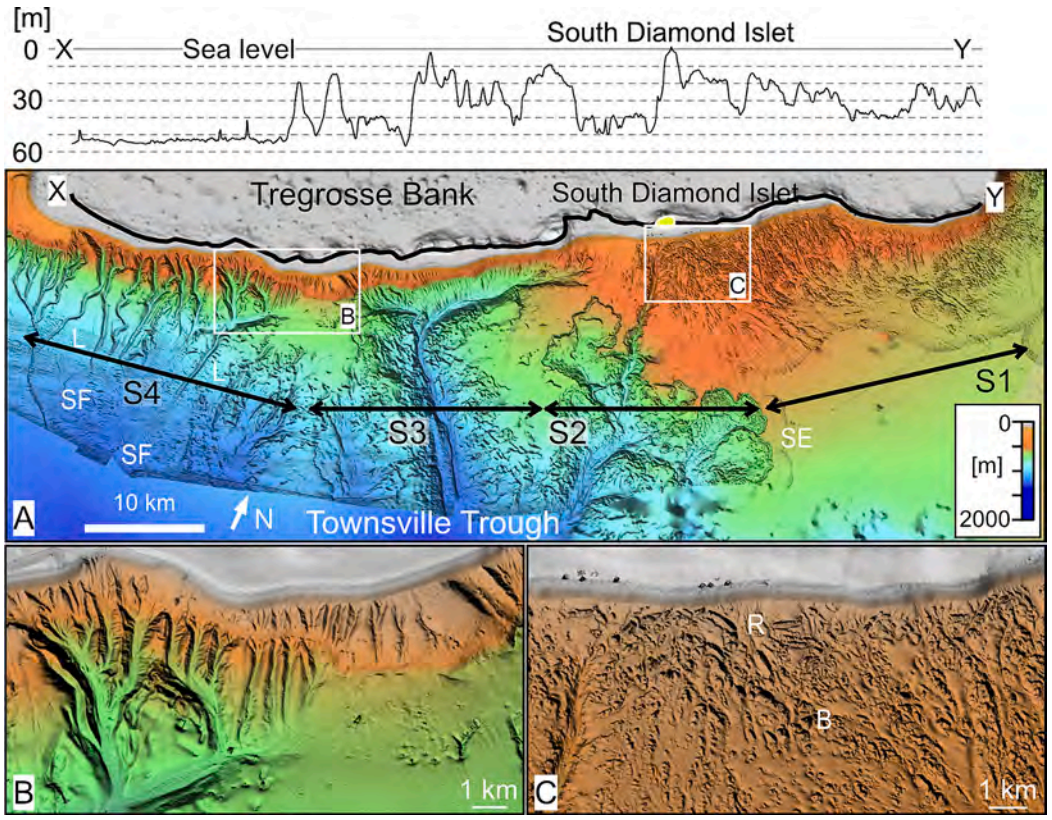

Fig. 2. **A**: Sea-floor morphology along the southern flank of Tregrosse Bank. The black line (X-Y) along the bank margin indicates the position of the section along the highest elevations in the platform rim area. The differences in the sea-floor morphology and features south of the bank allow the subdivision of the slope into four segments (S1 – S4). White rectangles mark the extension of detail views in the lower part of the fig. L: Channel levee; SE: Scalloped edge; SF: Submarine fan. **B, C**: Detailed map views of corresponding areas shown in A. B: Block; R: Ridge; TE: Terrace edge which lines up with the edge of the drowned Miocene platform. See text for discussion.

using the structure-from-motion algorithms of Pix4D (Pix4D Corp.) allowed for the generation of textured digital terrain models.

Sediment sampling was carried out with a box corer (footprint of 40 × 40 cm) and a gravity corer. The sediment texture of the loose (unlithified) sediment was described by applying the Dunham (1962) classification for carbonates. Grain-size distributions were determined every 2 cm down core with a laser-diffraction particle-sizer (Sympatec HELOS/KF Magic; range 0.5/18 to 3200 µm, 32 grain-size classes). Before measurement, samples (1.5 cm^3 each) were suspended in water using tetra-sodium diphosphate decahydrate as a dispersing agent. To ensure the accuracy of measurements, an in-house grain-size standard was measured daily (standard deviation of mean grain size 1.02 µm). Grain-size statistics are based on the graphical method (Folk and Ward, 1957), calculated using Gradistat (Blott and Pye, 2001).

The age model for gravity cores SO292_90GC (17°59.716′S / 150°28.265′E / 999 m) and SO292_34GC (18°03.988′S / 150°28.058′E / 1143 m) is based on stable oxygen isotopes and radiocarbon dates. Samples were wet-sieved and 12 specimens of the planktonic foraminifera *Globigerinoides ruber* were selected from the size fraction >250 µm. Stable oxygen isotopes were analyzed at the Leibniz Laboratory for Radiometric Dating and Stable Isotope Research at the Christian-Albrechts-University of Kiel, Germany with a Finnigan MAT 253 mass spectrometer coupled with a Carbo-Kiel IV device for CO_2 preparation from carbonate samples. The accuracy of stable isotope measurements is reported by the lab to be better than ±0.08 ‰. Radiocarbon ages were measured on mixed platonic foraminiferas selected from the sieve fraction >250 µm (Table 1) by Beta Analytics (Florida, USA); calibration was done using Calib (v.8.1.0, Stuiver and Reimer, 1993) and the Marine20 calibration curve (Heaton et al., 2020). The local reservoir age is unknown and therefore regarded as $\delta R = 0$.

X-ray fluorescence (XRF) core scanner data were collected with an XRF Core Scanner III (AVAATECH serial No. 12) at the MARUM, University of Bremen, Germany. Measurements were done every centimeter down-core over a 1 cm^2 area with a down-core slit size of 12 mm using generator settings of 10 kV and 30 kV, a current of 0.035 mA and 0.550 mA, and a sampling time of 7 s. The data have been acquired by a SGX Sensortech Silicon Drift Detector (SiriusSD D65133Be-INF), the Topaz-X High-Resolution Digital MCA, and an Oxford Instruments 100 W Neptune X-Ray tube with rhodium target material. Raw data spectra were processed using Iterative Least square software (WIN AXIL, Canberra Eurisys).

4. Results and interpretation

4.1. The slope of the southern platform flank

This description of the platform slopes is focused on the southern flank of Tregrosse Bank where data coverage is best (Fig. 1). Lateral changes in morphological elements characterize this slope, which generally faces southeast towards the adjacent Townsville Trough up to 1640 m deep (Fig. 2). The following segment descriptions on the southern flank are numbered 1 to 4 from the northeast towards the southwest and west, and delineated by different morphological features (Fig. 2).

Segment 1 has a lateral width of about 24 km (Fig. 2). Here, the slope plunges from a water depth between 20 and 25 m to ca. 550 m. The maximum slope inclination is around 31° ca. 2.6 km seaward of the bank edge (Fig. 1B). The seafloor most proximal to the shallow bank edge is covered with ridges and blocks separated by channels that are 10 to 20 m deep and up to 300 m wide (Fig. 2A, C). The density of ridges and

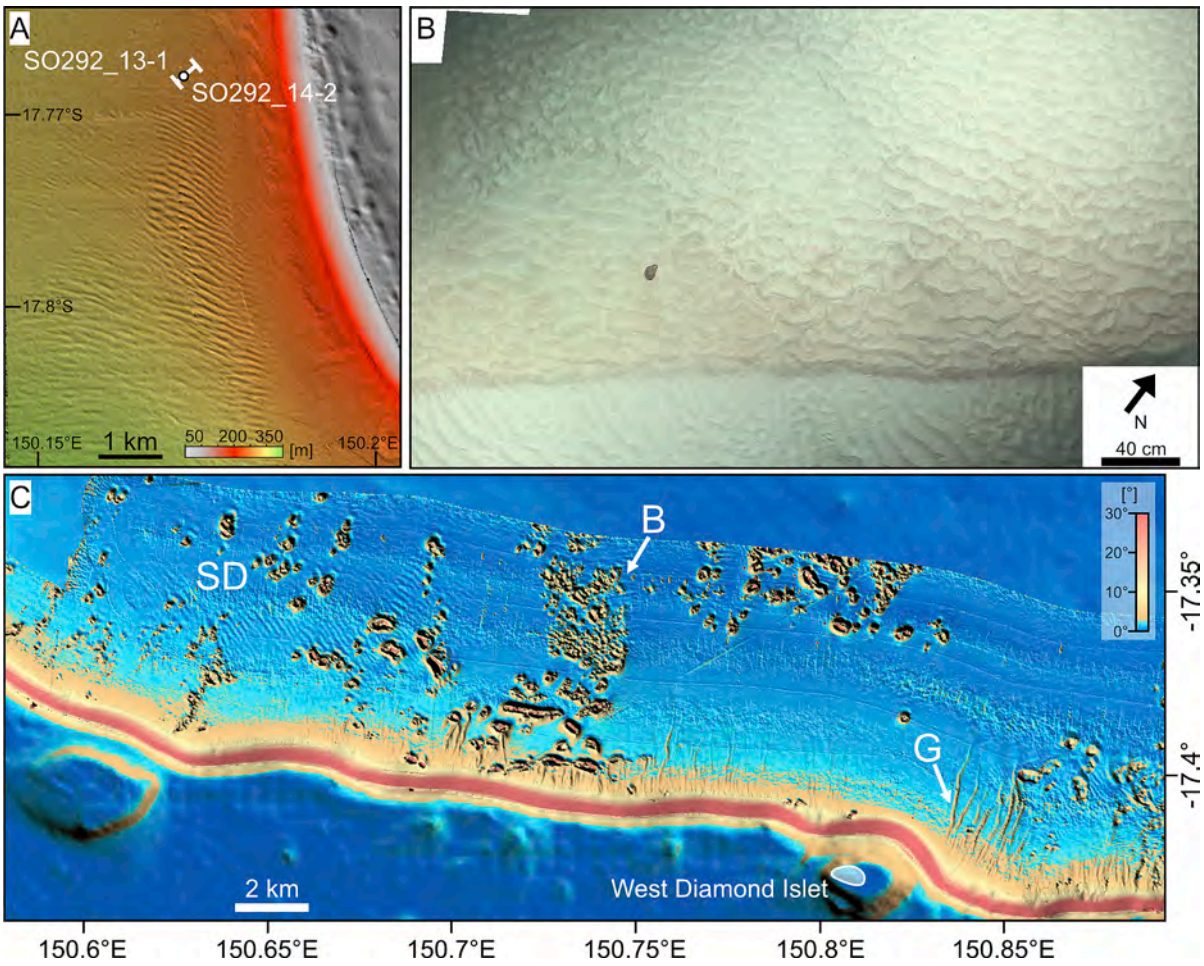

Fig. 3. **A:** Multibeam data of the sea floor west of Tregrosse Bank with submarine dunes and location of the OFOS transect as well as the location of sampling Station SO292_13–1 (see also Fig. 1 for location). **B:** OFOS imagery at station SO292_14–2 showing seafloor detail with different ripple generations. Water depth: 264 m. **C:** Detail of slope inclinations at the northern margin of Tregrosse Bank (see Fig. 1 for location). B: Blocks; SD: submarine dunes; G: gullies.

blocks decreases away from the bank edge, and the seafloor smooths out before dipping into the Townsville Trough ca. 30 km distance from Tregrosse Bank.

Segment 2 has a width of about 13 km. The bank edge lies at water depths of 20 to 50 m and also contains a 400 m wide sand cay surrounded by coral reefs (South Diamond Islet, Fig. 2A). The slope dips up to 32° over a distance of 1 km (Fig. 1B), before it flattens to ca. 0.5° when passing into a submarine terrace at a depth of about 520 m. Here, ridges and blocks cover the seafloor at the toe of the slope, and their abundance decreases away from the platform, but also towards the southwest, parallel to the bank edge. The gently dipping ca. 15 km wide submarine terrace ends at a sharp, scalloped edge. Farther south, the seafloor is terraced and characterized either by ridges and blocks or a smooth surface. A prominent, up to 150 m deep and 1.5 km wide submarine valley intersects segment 2. The basinward termination of this valley is not covered by our data, but the Australian gbr100 bathymetric data (Beaman, 2010) indicate that this valley connects with another valley within segment 3 ca. 37 km from the platform edge (Fig. 1A).

Segment 3 is 21 km wide and the bank edge lies at water depths of 10 to 50 m. The prominent morphological element of this segment is a large submarine valley, which in its upper reaches runs parallel to the platform slope before a bend deviates at 90° southward towards the Townsville Trough. Another tributary valley, also running parallel to the platform slope, merges with the main submarine valley. The extension of the valley towards the Townsville Trough cannot be fully assessed due to limited multibeam coverage, but the same valley is documented in the Australian gbr100 data (Beaman, 2010) at a water depth of 1500 m and a distance of 75 km from the bank edge with a width of ca. 3 km and an incised depth of ca. 30 m.

In contrast to segments 1 and 2, the slope of segment 3 in its upper part is stepped (Fig. 2A, B). From the bank edge down to ca. 275 m, the seafloor dips up to 34°, and subsequently passes into a seaward dipping terrace which terminates at a water depth of 450 to 480 m. The surface of the terrace can be traced as far west as the area near ODP sites 817 and 818 and is seen to correspond to the top of the drowned Middle Miocene bank, which is well defined for example to the north and west Tregrosse Bank (Fig. 1; Betzler et al., 2024). From the terrace down to the 600 m isobath, the slope has an inclination of up to 20°. From there on, the seafloor dips with values of around 1.5° into the Townsville Trough. The surface of the ca. 275 to 450–480 m terrace is dissected by gullies up to 1 km wide and 70 m deep. These erosional features merge downslope into larger gullies and valleys, which terminate in channel-levee and submarine fan complexes (Figs. 1, 2).

Segment 4 is about 27 km wide. Here the water depth of the platform edge is between 40 and 60 m. The upper slope, down to ca. 350 m dips with up to 31°. The middle part of the slope is dissected by sinuous submarine valleys, up to 200 m deep and 1.5 km wide. Valleys are oriented perpendicular to the platform edge, except for one which is roughly oriented parallel to the platform edge (Fig. 2A, B). In most cases, channels originate at the toe of the steep 300 m high cliff just below the bank edge, however, some upper channel reaches are located at shallower depths between 150 and 120 m. The ridges separating the channels have a smooth to crinkled surface. The lower reaches of most of the channels and valleys are not fully covered by the multibeam data,

however, within the limits of the mapped area two channels terminate in submarine fans.

Along the southern slope of Tregrosse Bank, there seems to be a correlation between the rim and edge morphology of the carbonate bank and the general slope morphology. Where the toe of the slope is characterized by ridges and block fields, the platform rim is relatively elevated, and shallow which also encompasses the South Diamond Islet and surrounding reefs. The upper mouth of the submarine canyons within segments 1 to 3 appears to be positioned where there are passages between these elevated areas. Segment 4, which contains abundant submarine channels and valleys is characterized by the deepest bank edge depths. The submarine channels and valleys are therefore interpreted to be controlled by sediment export from the bank and so off-bank sediment export is acting as an erosive agent incising the submarine valleys.

4.2. The slope of the western and northern platform flank

West of segment 4, the flank of Tregrosse Bank changes orientation towards a general south-to-north direction and terminates in a submarine plateau at a water depth of 300 to 400 m which gently dips towards the west (Figs. 1, 2). Towards the Townsville Trough, the edge of this plateau is formed by the margin of the Miocene drowned carbonate platform (Betzler et al., 2024) at a water depth of 480 to 500 m. The west-facing slope of Tregrosse Bank, except for two submarine valleys in its southern part, is a generally smooth surface dipping basinward up to 28°. The seafloor of the plateau adjacent to Tregrosse Bank and the plateau's edge is covered by submarine dunes (Fig. 3A). Submarine dunes are 3 m high with a wavelength of 100 m. Crests are angled in response to the gentle relief of the submarine plateau, which is interpreted to be the result of the diffraction of a northeast-directed bottom current sweeping around Tregrosse Bank.

Seafloor photography along a 432 m long transect across the submarine dunes (station SO292_13–1, depth 256–260 m, see Fig. 3A for location) shows the presence of a rather intricate pattern of ripples (cm-sized) and megaripples (10s of cm-sized) superimposed on the larger dunes also with apparently differing sediment characteristics (Fig. 3B). Sedimentary characteristics are inferred as there are well-defined seafloor areas with white to light gray colors, while others are rather light brown to yellow. The lighter-colored sediment is arranged in straight-crested to linguoid ripples. Ripple crests roughly show an east-west orientation, and the steeper ripple flanks point towards the south. The darker sediment forms straight-crested megaripples covered by smaller ripples with sinusoid crests and linguoid ripples. Megaripples migrate towards the southeast, and the ripples covering the megaripples indicate a more south-directed current flow. A box core sample (station SO292_14–2, Fig. 3A) was recovered from the lighter-colored sediment, which has a skeletal packstone texture. Components include planktonic foraminifers, abundant 5 mm to 1 cm large lithoclasts, pteropods, solitary corals, bryozoa, benthic foraminifers (including *Calcarina*), planktonic foraminifers, and isolated rounded pumice clasts.

Although there is only limited data coverage, the northern flank of Tregrosse Bank is not as strongly sculpted as the southern bank margin (Fig. 1A). Slope angle reaches up to 40° (Fig. 1B) and three morphological elements are recognized. Furrows and gullies originating at a middle slope position are in areas between elevated bank margins, including the West Diamond Islet (Fig. 3C). Additionally, the lower and distal slope is covered by blocks surrounded by circular moats. Finally, the seafloor in parts of the distal slope on the deeper submarine plateau surface and around these blocks exhibits submarine dunes with wavelengths of around 200 m and elevations of 4 to 5 m (Fig. 3C).

4.3. Platform edge and upper slope facies

The morphology and main sediment compositional variations along an 814 m long OFOS transect the upper slope of Tregrosse Bank in segment 4 (station SO292_38–1) is shown in Fig. 4 (Fig. 1 for location). The platform edge lies at a depth of 55 to 60 m. Photic carbonate production, mainly by live *Halimeda* and red algae (abundant rhodoliths) is observed down to a water depth of 203 m. The large benthic foraminifer *Cycloclypeus* is a frequent component in the same zone. *Halimeda* flakes, i.e. debris of dead *Halimeda*, can be traced down to a depth of 319 m. Between 203 and 319 m the substrate is a mosaic of rocks and fine-grained sediment. Rocky areas are colonized by some encrusting red algae and by soft corals. Other components are fragments of echinoidea and other bioclasts which cannot be determined further due to the photographic resolution. Farther downslope, below 319 m, the sediment is fine-grained, with burrows, ripples, and sparse azooxanthellate soft corals.

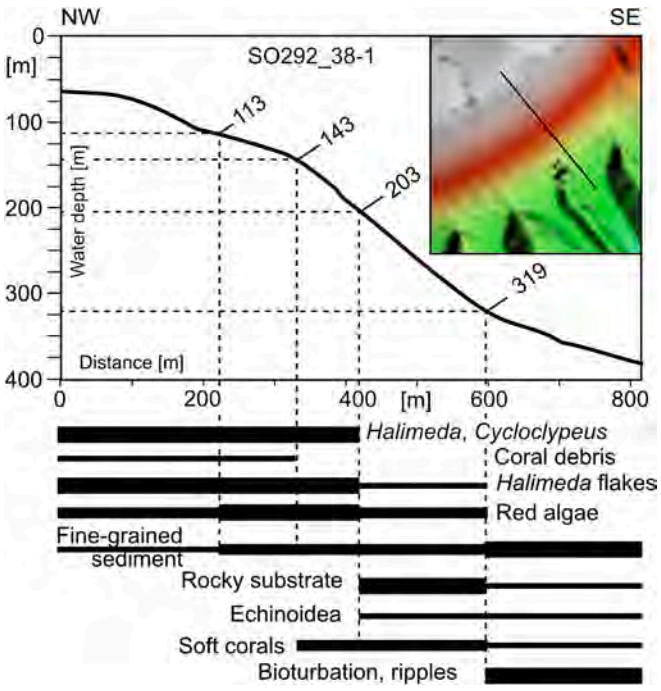

Fig. 4. Distribution of main components and features of the upper slope of Tregrosse Bank based on OFOS photography. Red algae between ca. 100 and 143 m of water depth are mostly rhodoliths. Fine-grained sediment is mud to silt-sized. The location of the transect is shown in Fig. 1. (For interpretation of the references to colour in this figure legend, the reader is referred to the web version of this article.)

4.4. Mass transport complexes

Multibeam and OFOS data show that there are two types of mass-wasting processes acting along the slope of Tregrosse Bank: submarine rockfalls and calciturbidite systems. Submarine rockfalls as block fields are located at two distinct morphological locations: at the toe of the upper slope of the active Tregrosse platform and at the lower slope, several kilometers away from the bank edge. Both block fields are not connected. Calciturbidite systems are point-sourced and form channel and fan systems.

4.4.1. Submarine rockfalls and scarps

The seafloor at the toe of the slope in segments 1 and 2 between 290 m and 490 m is paved with ridges and blocks up to 820 m wide and up to 50 m high (Fig. 5A). The OFOS imagery (station SO292_31–1, Figs. 1 and 5A for location) reveals that the blocks consist of different carbonate rock types (Figs. 5B-D). One type has a texture like a clast-supported breccia (Fig. 5B). Clasts are subangular to rounded and vary in size from several centimeters to tens of centimeters. The smaller rounded clasts in some cases are broken and appear to have a faint structure of

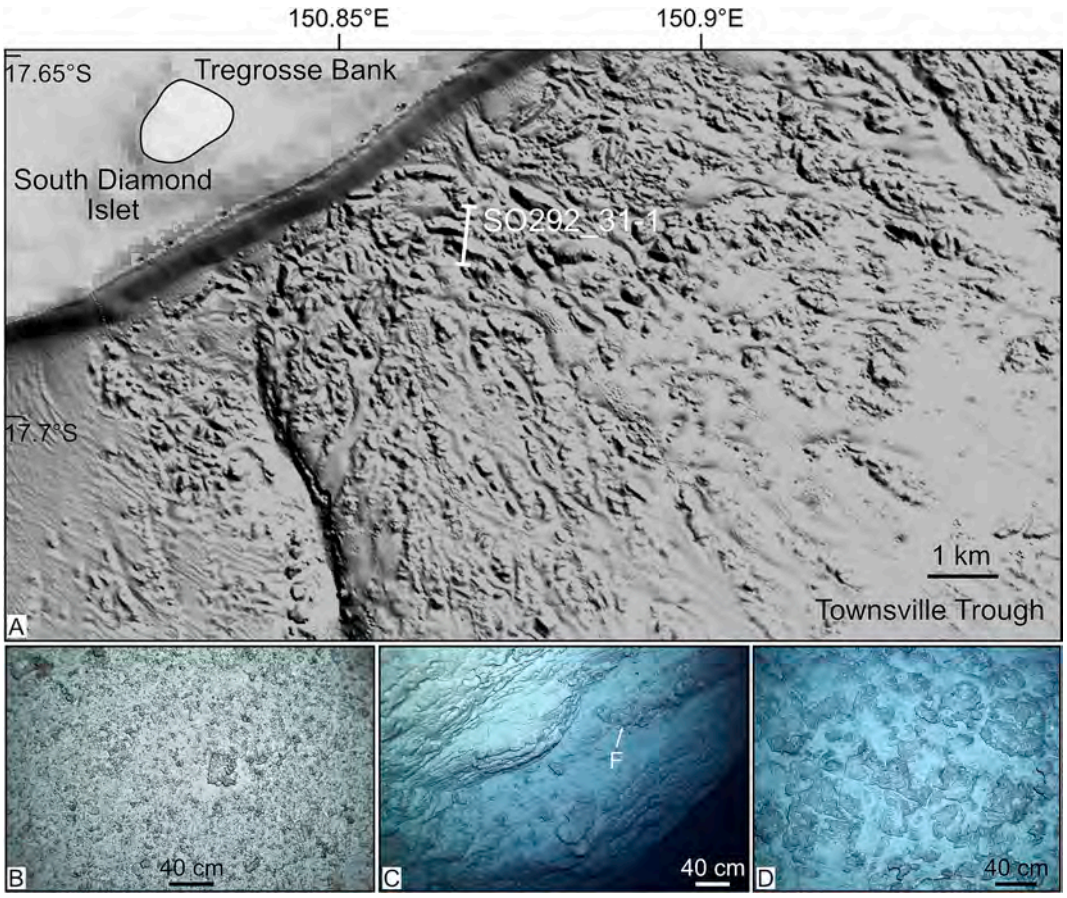

Fig. 5. **A:** Shaded relief (based on multibeam data) of the ridge and block field lining the platform slope in segments 1 and 2. **B:** OFOS image of the surface of a block at station SO292_31–1 (water depth: 352 m). The rock consists of a breccia with rounded and sub-rounded pebble-sized clasts. A more detailed view is provided in Supplementary Fig. 1. **C:** Alternation of massive beds and conglomeratic intervals containing boulder-sized rounded clasts. A more detailed view is provided in Supplementary Fig. 1. Water depth: 340 m. **D:** Block consisting of sub-rounded boulders embedded in a finer-grained matrix (water depth: 360 m). Note that some boulders are fractured (F; see Supplement 1 for more detail).

internal concentric layers (Supplementary Fig. 1). Another rock type is represented by bedded conglomerates that are arranged in intervals with faint and poorly pronounced bedding alternating with more massive beds that lack large components (Fig. 5C, Supplementary Fig. 1). Larger clasts in the conglomerates appear to be reworked rocks with a conglomeratic texture. Such beds are wedge-shaped and fractured internally (Fig. 5C, Supplement 1). Fractures do not propagate out of the beds. Conglomerates contain boulders larger than 50 cm. Boulders are rounded to subangular.

A further rock type contains subangular boulders with sizes ranging between several centimeters to >50 cm (Fig. 5D). Boulders are embedded in a matrix, and some of the boulders are fractured.

Blocks are surrounded by mounded and well-layered deposits which are separated from the blocks by depressions (Figs. 5A, 6). Mound-shaped bodies and depressions are interpreted to result from the action of bottom currents, with the depression formed by erosion or winnowing around the blocks and the mound-shaped sediment packages representing drift bodies. Block size decreases away from the platform slope. Stratified sediments surrounding and embedding the blocks decrease in thickness downslope and finally wedge out thus exposing deposits with a high acoustic impedance.

The larger elongated blocks are interpreted as parts of the platform edge and platform slope transported downslope by large-scale gravitational collapse. This is based on the observation that the blocks consist of breccias and conglomerates reminiscent of facies usually located at the upper slope of a carbonate platform, as is also the case for Tregrosse Bank (Fig. 4). The smaller rounded clasts with concentric layering could be the remains of rhodoliths.

The other block field is in segment 2 at a depth of 680 to 860 m (Fig. 7). The field is delimited upslope by up to 5 km wide and 80 to 125 m high arcuate head scarps at depths between 520 and 680 m. The head scarps dip up to 63° down to a water depth of 600 to 680 m. The OFOS imagery of station SO292_29–1, conducted as a transect across a scarp and a toe of the scarp (Figs. 6, 7) shows that there is no recent sediment cover in the area, except for some isolated ripples consisting of coarse-grained bioclasts. Rocks are bioturbated and fossil *Thalassinoides*-like burrows cover the surface of the bed exposed at the top of the scarp (Fig. 8A). This bedding plane corresponds to the high-impedance reflection displayed in Fig. 6. The scarp exposes fractured beds (Fig. 8B). At the base of the scarps, 1 to 3 km wide block-covered terraces shape the seafloor (Fig. 7A). Blocks are scattered on these terraces and consist of the same rocks as the ones forming the scarps, i.e. bioturbated and bedded limestones.

The subsurface depth of the detachment surface of the submarine slope instabilities cannot be determined using Parasound data given the poor depth of penetration (e.g. Fig. 6). No seismic profiles exist for the slope part of Tregrosse Bank discussed herein. But further to the west, crossing ODP site 817, seismic and well data indicate that at the base of slope instabilities there the detachment surface lies 400 to 430 m below the seafloor (Betzler et al., 2024). Further, a seismic line acquired by Shell (Line 1129, see Fig. 1 for location), albeit lying outside the area studied herein, shows a similar image with a detachment surface positioned ca. 0.4 to 0.6 s (ca. 450 to 500 m) below the seafloor (Fig. 7B). Given the comparable depth positions of the base of the slope

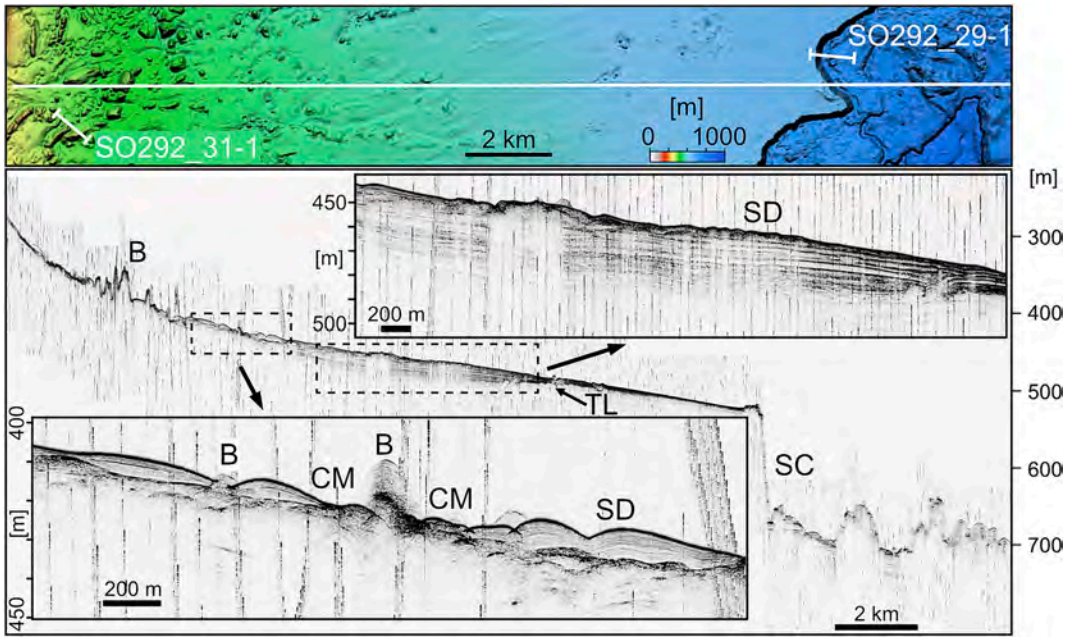

Fig. 6. Parasound profile of the southern slope of Tregrosse Bank with details. Blocks (B) are surrounded by well-bedded deposits arranged into submarine dunes (SD) documenting the effect of bottom currents. Around the blocks, there are current moats (CM). Layered deposits are therefore interpreted as drift deposits. The submarine cliff (SC) exposes bioturbated rocks (Fig. 8) in an OFOS transect located 576 m more to the east (station SO292_29–1). The top of the lithified succession is a roughly horizontal reflection (TL), which can be traced below the drift deposits.

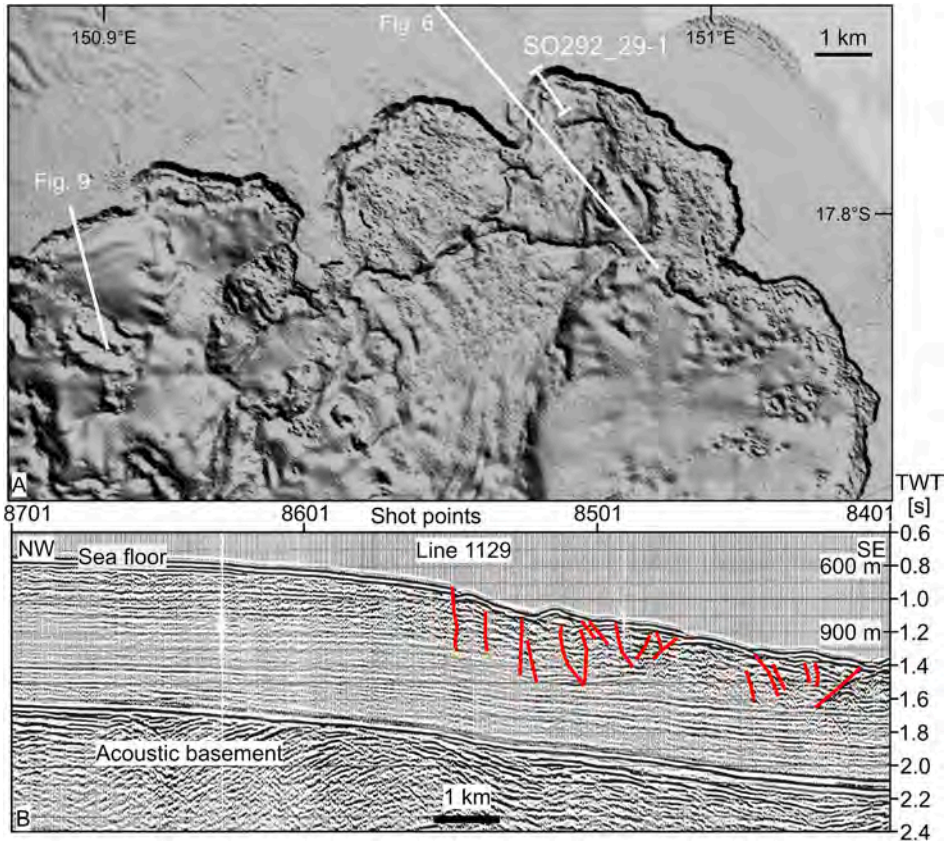

Fig. 7. A: Seafloor morphology of the lower slope in segment 2 with the track of OFOS survey SO292_29–1 (seafloor photographs shown in Fig. 8). **B:** Shell seismic line 1129 (survey ID ENO0260473) lying ca. 36 km east of the structures shown in A (exact location of the line shown in Fig. 1) with interpretation of structural deformation (red lines). The base of the sediment displacement appears to be rooted ca. 0.3 to 0.4 s TWT below the seafloor. (For interpretation of the references to colour in this figure legend, the reader is referred to the web version of this article.)

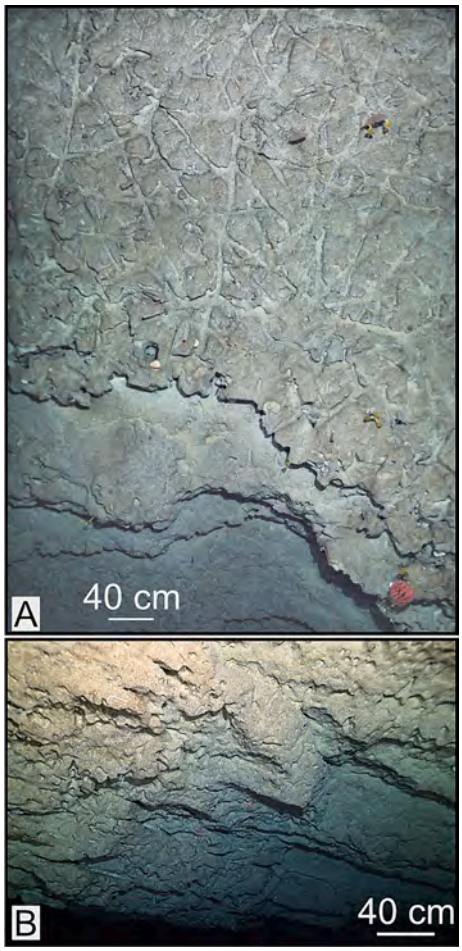

Fig. 8. OFOS seafloor photographs from station SO292_29–1 (location in Figs. 6 and 7). **A:** Upper termination of head scarp exposing bedded rocks. The bioturbated surface (water depth 540 m) is the top of the lithified succession as imaged in the Parasound profiles (Fig. 6). **B:** Head scarp exposing bedded and fractured rocks (water depth: 550 m).

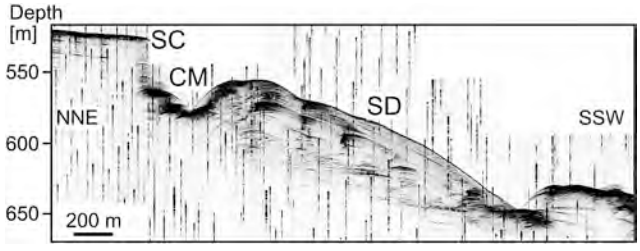

Fig. 9. Northeast to southwest running parasound profile of the head scarp and drift deposits covering the terrace in front of the main scarp (see Fig. 7 for location; CM: current moat; SC: scarp; SD: submarine dunes).

instabilities, it is proposed that they are rooted at the same lithological heterogeneity which is also present in the herein studied area,

Within segment 2, some of the lower slope terraces have a smoother surface covering areas of several hundred meters to kilometers in distance. Parasound data show that there the seafloor has a convex-up morphology and is separated from the scarps and blocks by depressions (Fig. 9). Internally deposits are layered, displaying 100 to 200 m sub-parallel reflections with inclined bedding reminiscent of submarine dunes. These sediments are therefore interpreted as contourite drifts interspersed within the block field.

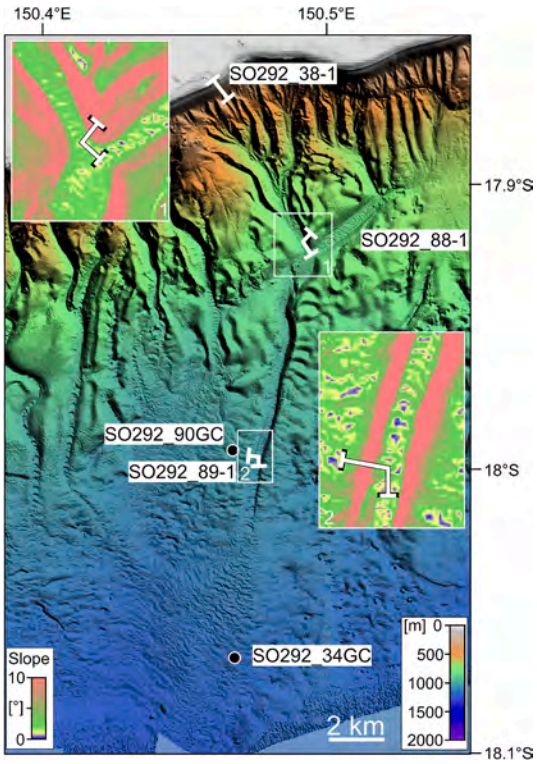

Fig. 10. Multibeam map of a channel and submarine fan system at the southern slope and lower slope of Tregrosse Bank (see Fig. 1 for location) with the position of OFOS transects and core locations discussed in the text. Insets present the seafloor angle variations to highlight the submarine dunes at the channel floor.

4.5. *Submarine channel and fan systems*

4.5.1. *Upper valley*

To document the calciturbiditic and the carbonate source-to-sink system, one submarine valley has been investigated by box corer, gravity corer, and OFOS at several points along its course (Fig. 10). The upper end of the valley lies at a depth of 320 m. Further upslope, the valley opens to the mostly unsculptured upper bank slope below the bank edge at a depth of 62 m (Figs. 1, 4). The submarine valley has a length of 16 km, and several tributaries merge with this valley over its course. The sinuosity of the submarine valley generally is low. This also applies to most other channels in the area, although several are characterized by some bends (Figs. 1, 2, 10).

One major tributary, joining the main valley 6.9 km downslope from the upper valley mouth, has a northeast to southwest orientation and appears to cross the main valley. It is therefore interpreted as structurally controlled, as this orientation corresponds to the direction of normal faults at the northern margin of the Townsville Trough (Struckmeyer and Symonds, 1997).

To characterize the flanks of the submarine valley in the middle part of its course, a 910 m long OFOS transect was recorded in a depth of 766 to 853 m at station SO292_88–1 at the eastern valley flank (Figs. 10, 11). Deposits are fine-grained in the upper flanks of the valley with the seafloor covered by linear ridges several centimeters high and wide, and up to several meters long (Fig. 11A). Xenophyophores, surrounded by several cm-wide moats locally colonize the substrate. The more elevated and steeper flanks of the moats are consistently facing southwest (ca. 205°), which is interpreted to reflect a southwest-directed bottom current. The linear ridges are oriented in a northeast to southwest direction (215°), which also indicates shaping by a bottom current flowing in this generally southwest oriented direction.

The lower parts of the valley flank, where the slope dip is steepest

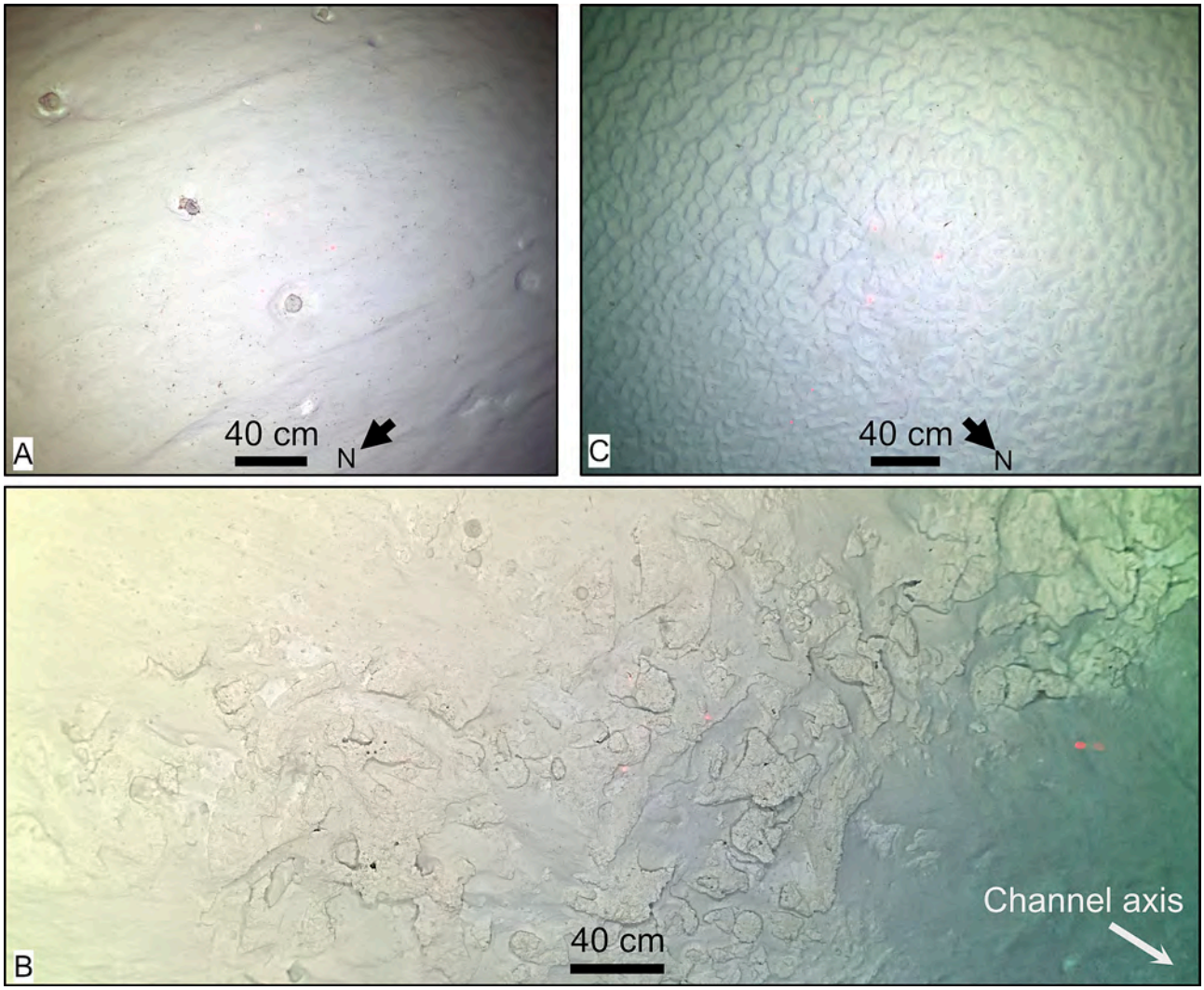

Fig. 11. OFOS seafloor photographs from Station SO292_88–1 (see Fig. 10 for location). **A:** View of the deposits at the shoulder of the incised submarine channel. Sediment is fine-grained and the sediment surface is sculptured with longitudinal ridges a few centimeters high, interpreted as shaped by bottom-currents. Several specimens of xenophyophores (?) populate the seafloor. Note the circular depressions around the specimens which are interpreted to reflect current erosion (water depth: 780 m). **B:** Channel flank exposing bioturbated and partially lithified to lithified deposits (water depth: 798 m). **C:** Valley floor covered by ripples (water depth: 845 m).

(ca. 30°), expose faintly bedded and partially lithified sediment deposits with a nodular appearance, which is interpreted to be a consequence of differential lithification of burrows (Fig. 11B). We therefore propose that at these steeper places of the valley flanks, erosion cuts down into older deposits that have already undergone a certain amount of burial (10s of meters) to result in partial lithification.

The main valley floor is covered by megaripples (Fig. 10). The bent bedform crests are oriented with an angle of 53° to 61° in relation to the valley flanks. In the tributary (Fig. 10) the angle between the crests and the flank of the valley is from 55 to 85°. The wavelengths of the megaripples are from 50 to 80 m, with the crest elevation at a maximum of 1 m above the surrounding seafloor. Seafloor photography shows the channel floor is covered by linguoid ripples (Fig. 11C). Ripple orientation indicates a south-directed sediment transport inside the valley itself.

4.5.2. *Lower valley: channel levee and fan complex*

The submarine valley terminates in a channel-levee and submarine-fan depositional system. The segment with channel levees is 5.5 km long (Fig. 10). A 518 m long OFOS survey SO292_89–1 was performed in depths between 996 and 1041 m across the western levee and into the central part of the lower valley. The top of the levee lies ca. 6 to 10 m above the surrounding seafloor; from the top of the levee to the valley floor the elevation is 36 to 37 m. The levee has a gentle outside shoulder and dips with >30° in the middle part of its flank. Some parts of this flank expose beds that appear partially lithified similar to observations further up the channel (Fig. 12A).

The valley floor itself is covered by trough-shaped megaripples with wavelengths of 100 to 150 m, and a crest elevation of up to 2 m (Fig. 12B). Megaripple surfaces are covered by straight-crested to linguoid ripples. Ripple orientation is not consistent, pointing in varying directions.

The western and eastern levees either side of the lower valley have different shapes and cross sections (Figs. 10, 13). The eastern levee surface has an irregular morphology, with 1 km wide and 30 to 40 m deep depressions. The surface of the western levee is shaped by regular and arcuate sediment waves. The upper ca. 40 m of the sediment succession of the levees are well imaged in Parasound data (Fig. 13A). Two acoustic facies make up the succession. An upper, 4 to 5 m thick unit is acoustically transparent or contains a faint layering. This unit laterally changes into facies with stronger and more irregular reflections. The lower acoustic facies display stronger, and locally discontinuous

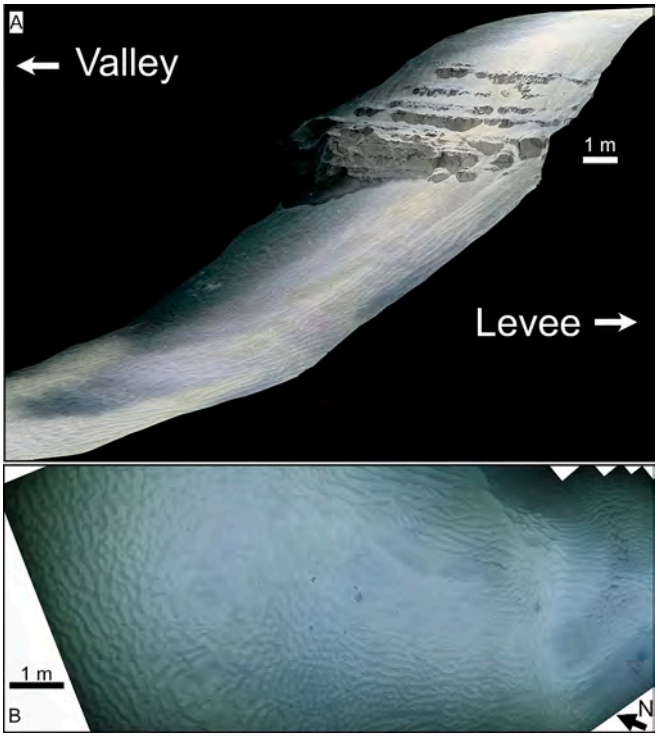

Fig. 12. OFOS seafloor photographs at Station SO292_89–1 (see Fig. 10 for location). **A:** Flank of the levee exposing layered and bioturbated partially lithified to lithified deposits (water depth: 1032 m). **B:** Channel floor covered by megaripples and ripples (water depth: 1039 m).

reflections. In part, these acoustic facies also show patterns indicative of low-amplitude submarine dunes, which migrated upslope along the western levee flank.

Downslope of the lower valley the submarine fan complex covers an area of approximately 31 km^2. It is up to 5 km wide with an elevation above the fan-surrounding seafloor of 16 to 20 m (Figs. 10, 13). The sediment surface of the fan is covered by low amplitude submarine dunes 1.5 to 6 m high, with a wavelength of 150 to 300 m and curved crests (Figs. 10, 13B, C). Parasound profiles crossing the fan display discontinuous and wavy cross-bedded layering indicating the stacking of submarine dune bodies. Submarine dunes decrease in size from the proximal to the distal part of the fan. A longitudinal section of the submarine fan (Fig. 13D) shows the upper ca. 20 to 30 m subsurface of the succession with upslope migrating dune bodies.

4.5.3. Channel levee and fan sediments

Core SO292_90GC (Fig. 14) recovered 3.8 m of the sediment at the flank of the western levee, ca. 640 m away from the channel axis, i.e. in an overbank position (Figs. 10, 13A). The mottled deposits are gray below 120 cm, and light gray to light brown between 120 and 12 cm. The uppermost part of the sediment succession is red to brown. The sediments have a wackestone texture throughout. At 55 cm and 67 cm, there is a sharp base of two layers with a packstone texture; the layers are two centimeters thick. Mean grain size of the sediment is around 40 to 50 μm in the lower 158 cm and fines to around 20 μm in the remaining section. The fraction <16 μm makes up between 4 and 20% of the bulk sediment below 160 cm and has a maximum ratio of 39% at 145 cm (Fig. 14). Above 127 cm, this fraction fluctuates between 16 and 33%. The main components of the sand-sized and larger fractions are planktonic foraminifers, pteropods, and bioclasts. Minor components are echinoid debris, mollusks, bryozoan debris, and debris of the large benthic foraminifer *Marginopora*, together with some specimens of the reef-dwelling foraminifer *Calcarina*.

Strontium (Sr) XRF counts and the proportion of the <16 μm grain size have the same overall trend, with higher values in the upper part of the succession (Fig. 14). There is, however, a minor offset for the base of the increase which lies at 162 cm for the Sr values and 160 cm for the fine fraction. The red interval in the upper 12 cm of the core is due to red staining and red crusts around bioclasts. The interval correlates with an iron (Fe) peak in the XRF data (Fig. 14). The Fe and potassium (K) values throughout the core vary in parallel, with two exceptions: between 85 and 71 cm the K counts are slightly more elevated, whereas the Fe counts show a general decrease. Between 15 and 8 cm, the Fe curve shows a peak corresponding to the interval of red sediment, but the K values largely remain unchanged.

Variations of the stable oxygen isotope ratios and five radiocarbon ages allow us to present an age model of the stratigraphic succession recovered in core SO292-90GC (Figs. 14, 15 Table 1, Suppl. 2). A sample at a core depth of 170 cm yields an age of 13.99 ± 0.21 ka cal. BP, a sample at 140 cm an age of 10.47 ± 0.16 ka cal. BP, a sample at 100 cm an age of 9.73 ± 0.17 cal. BP, a sample at 40 cm an age of 2.60 ± 0.16 ka cal. BP, and a sample at 10 cm 0.85 ± 0.14 ka cal. BP (Table 1).

The average sedimentation rate for the last 10 ka is around 10.3 cm kyr^{-1}. However, with the data available it is not possible to provide an exact age for the base of the core, which is here tentatively placed at 55 ka BP, based on the correlation of the oxygen isotope curves. The heaviest values of $\delta^{18}O$ are measured at a core depth of 190 cm. In the lower interval of the core, the oxygen isotope values have an upward trend towards heavier values, which is interpreted to reflect the stage of global cooling preceding the Last Glacial Maximum (LGM, Fig. 15).

The variation of Sr counts in core SO292_90GC appear to trace the sediment export from the shallow water part of the carbonate bank. This is in line with data shown by Counts et al. (2019) and Jorry et al. (2020) from carbonates in the Mozambique Channel, where the shallow water aragonitic input has been linked to Sr concentration in the sediment, with high Sr values correlating to high aragonite concentrations. The lowest Sr counts are in sediments deposited before 13 ka BP. This correlates with the time interval when Tregrosse Bank was exposed due to lowered global sea level. The bank edge, which today lies at a water depth of 50 to 60 m was flooded between 13 ka BP and 10 ka BP (Hinestrosa et al., 2022; Fig. 15). The highest Sr values are further interpreted to characterize the time when the platform was in the optimal water depth for carbonate production with a maximum export rate of shallow-water components, before deepening further due to the maximal Holocene sea-level rise.

Core SO292_34GC recovered 3.22 m of sediment (Fig. 14) approximately 5 km down from the upslope fan limit at a depth of 1551 m (Figs. 10, 13C). The succession consists of three parts. The lower part (180 to 322 cm) is an alternation of light brown grainstone and gray wackestone to packstone. Up to 13 cm thick fining-upward grainstone layers with abundant planktonic foraminifers and pteropods as well as some benthic foraminifers, ostracods, and bioclasts (including mollusk and bryozoa debris) have a sharp base and are interpreted as turbidite layers. Between 180 and 50 cm, the core consists of a gray to light brown wackestone to packstone with abundant planktonic foraminifers and pteropods, as well as some benthic foraminifers, ostracods, volcanic glass, sponge spicules, and mollusk and bryozoan debris. The upper part of the core is a red to brown wackestone to packstone dominated by planktonic foraminifers and pteropods, also containing benthic foraminifers, and debris of gastropods, echinoderms, and bivalves. The upper part is the finest-grained part of the core with mean grain sizes of 20 to 40 μm.

The variation of the Sr counts in the core follows this subdivision. In the lower part, the coarse-grained graded intervals are rich in Sr. Then Sr concentrations drop in the middle part of the core with the upper part of the core showing the highest Sr counts. The Fe and K counts after increasing upward from the core bottom are highest in the middle core interval. Counts of K drop towards the core top. Except for three peaks that correlate with the red layers, Fe values show the same trend.

Four radiocarbon ages together with the variations of stable oxygen

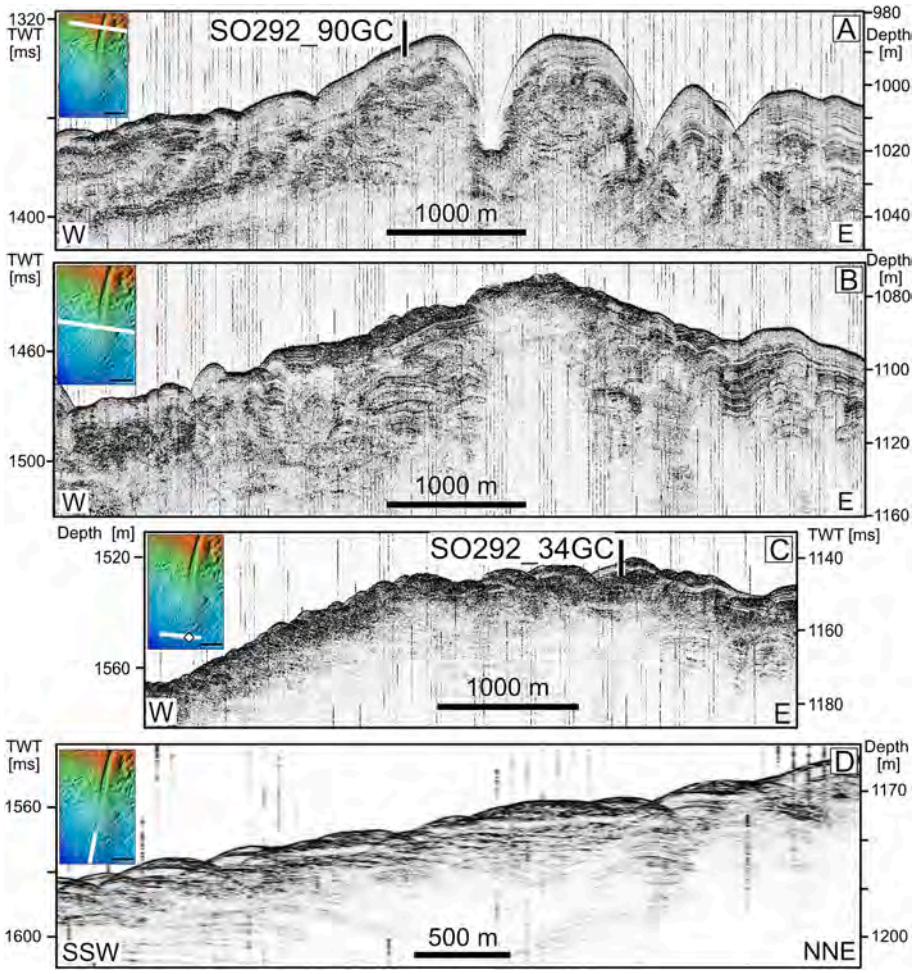

Fig. 13. Parasound profiles of the channel levee and fan depositional system (insets for location show the central part of Fig. 10). **A:** Cross section of the channel-levee system with the position of gravity core SO292_90GC. **B:** Cross section of the proximal fan. **C:** Cross section of the distal fan. **D:** Longitudinal section of the distal fan with antidunes. Inlays in A-D indicate the locations of sections.

isotope ratios (Table 1, Fig. 14) are used to propose an age model for the succession of core SO292_34GC. The oxygen isotope minimum is located at a core depth of 107 cm where a radiocarbon age of 26.84 ± 0.32 ka cal. BP was determined. A radiocarbon age of 9.29 ± 0.16 ka cal. BP was determined at 47 cm core depth, 4.21 ± 0.18 ka cal. BP at a core depth of 27 cm, and 0.48 ± 0.14 ka cal. BP at a core depth of 2 cm (Table 1). Consequently, the lower part of the core is interpreted to document sedimentation preceding the LGM, which is registered at a core depth between ca. 85 and 110 cm. As is the case for core SO292_90GC, the amount of Sr registered in the XRF data is interpreted to reflect the export of platform-derived material, with two core intervals displaying elevated values: a lower interval that has been deposited during the sea-level fall preceding the LGM, and an upper interval recording the flooding of Tregrosse Bank (Fig. 15). Average sedimentation rate for the last 9.3 ka is 5.4 cm kyr^{-1}.

The variations and the peaks in iron counts in both cores do not correlate in time (Fig. 15). As the iron-rich layers are well bracketed by radiocarbon ages (Fig. 14), incompleteness of the sedimentary succession as a potential explanation for the apparent diachrony can be ruled out. Variations of iron and potassium concentrations may be used to trace aeolian versus aquatic input of lithogenic components in marine carbonates (Kunkelova et al., 2018; Lindhorst et al., 2019). For most parts of the analyzed cores, values for both elements co-fluctuate, except for the iron peaks in the youngest part of the cores. Based on this, we rule out that the peaks of the iron content do reflect direct input, for example by wind.

Instead, we propose the elevated iron contents in the red layers to reflect the reworking of paleosols during the flooding of Tregrosse Bank. In such a scenario, wind-derived iron would have been accumulated and concentrated in paleosols on the emerging platform, i.e. islands, during the last global glacial sea-level lowstand. Although Tregrosse Bank most of the time lies in the trade wind belt, intense atmospheric low-pressure areas today also trigger dust storms transporting dust several hundreds of kilometers into the Coral Sea (De Deckker et al., 2014). This process may have been more intense in the past: the bank today lies in the belt of the monsoonal tropics that are reported to have been generally dryer from 30 to 17.5 ka (Williams et al., 2009). Dryer conditions in northern Australia and increased aeolian flux around the LGM have also been reported from lagoonal sediments on Cape York Peninsula (Rivera-Araya et al., 2022) as well as for northern and eastern Australia in a broader frame (Petherick et al., 2009; Fitzsimmons et al., 2013). Given that Tregrosse Bank is located 300 km away from the present-day coastline, a distance reduced to 180 km during the glacial lowstand of sea level, dust export to the Coral Sea, and accumulation on the sub-aerial exposed bank are deemed likely.

5. Discussion

To a certain degree, the flanks of Tregrosse Bank show the typical windward to leeward or up-current to down-current morphological differences known from other carbonate platforms (Schlager, 2005). A steep slope characterizes the windward flank of the bank, and gentler

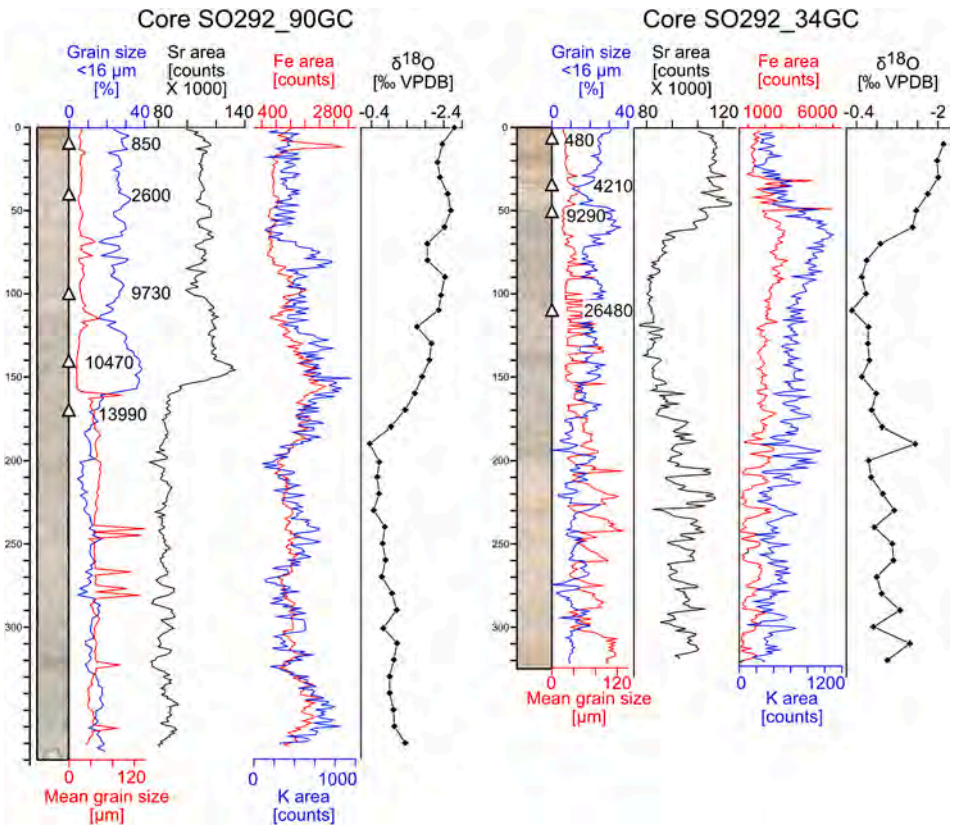

Fig. 14. Sedimentary successions of cores SO292_34GC and SO292_90GC. Triangles indicate the positions of age tie points based on radiocarbon dating, ages are given in ka cal. BP.

dipping flank to leeward. This is best explained by the sediment export pattern from the inner bank towards the leeward slope and the resulting platform-edge progradation. Although such shallow-water sediment export is minor today at Tregrosse Bank because the platform is at mesophotic depths (50 to 70 m, Reolid et al., 2024), it has been documented for the western slope by the seismic imaging of bank edge progradation in seismic lines crossing the flank of the bank (Betzler et al., 2024).

For the northern flank of the platform, a certain shallow-water sediment export is also documented by furrows and gullies (Fig. 1B, 3C), however, in contrast to the western flank, numerous block fields cover the seafloor. Together with the occurrence of the submarine dunes in the lower part of the slope, this is taken as an indication that sediment winnowing plays a certain role in the slope over-steepening and -destabilization by reducing or inhibiting sediment deposition at the toe of slope.

The windward and up-current flank of Tregrosse Bank, i.e. the southern flank, currently is in a state of disintegration. Our data indicate that three different and apparently unrelated processes act along the same carbonate platform slope, leading to the dismantling of the bank through slope erosion, slope destabilization, and submarine rockfalls (Fig. 16).

Slope erosion is reflected by the submarine valley to fan depositional systems. Sandy turbiditic flows, i.e. flow events focused in the submarine channels with the sand-sized suspension load mostly deposited in the submarine fans. Fine-grained strontium-rich deposits (i.e. rich in aragonite) without any apparent layering occur in the fan but also on the channel levee. The Holocene sedimentation rate in the levee area (10.3 cm kyr^{-1}) is roughly doubled compared to sedimentation in the fan (5.4 cm kyr^{-1}, Fig. 14), which could be a consequence of channel-related, focused flows winnowing the fines. Such flow is indicated by the ripple and megaripple cover of the channel floor in the proximal fan (Fig. 12B). It remains open for discussion if the fine-grained platform material is exported in the form of suspension load in discrete flows or if the fine-grained components are deposited as a sort of hemipelagic rain, i.e. that material from the platform is exported in form of a nepheloid suspension at a density contrast in the water column, as has been reported from other carbonate platforms (Wilson and Roberts, 1995). Regardless of the answer to this question, radiocarbon and oxygen isotope data show (Fig. 15) that turbidites were mostly deposited during the sea-level lowering preceding the last glacial sea-level lowstand, i.e. the turbidites were formed during a phase of forced regression. Such a pattern of calciturbidite export during forced regressions was also noted from the deeply submerged Pedro Bank, a carbonate platform located in the Caribbean (Andresen et al., 2003). The erosion potential of the off-bank directed flows appears to be relevant, as the submarine valleys are up to 150 m deep. Available data, however, do not allow us to state when this process started in the past.

In slope segment 4, the submarine gullies and valleys are not linked to slope destabilization features (Fig. 2). This is different from slope segment 2, where the valley crosses the scalloped edge, and could be interpreted to be linked to the slope destabilization and a retrograde headward erosion. This is possibly also applicable to the large channel found in slope segment 3. The basal detachment surfaces of the submarine landslides are rooted ca. 400 m below the seafloor, which indicates that a lithological heterogeneity controls the slope instabilities. The ODP Site 817 stratigraphy, where the basal detachment level is imaged in a seismic profile, shows that it is in the Middle Miocene part of the succession where it corresponds to a peak in the gamma-ray log (Betzler et al., 2024). A process acting at the sediment surface, e.g. erosion by bottom current and related over-steepening of the slope, can therefore not be seen as the sole controlling factor for these seafloor instabilities.

Summarizing, processes at the slopes of Tregrosse Bank share

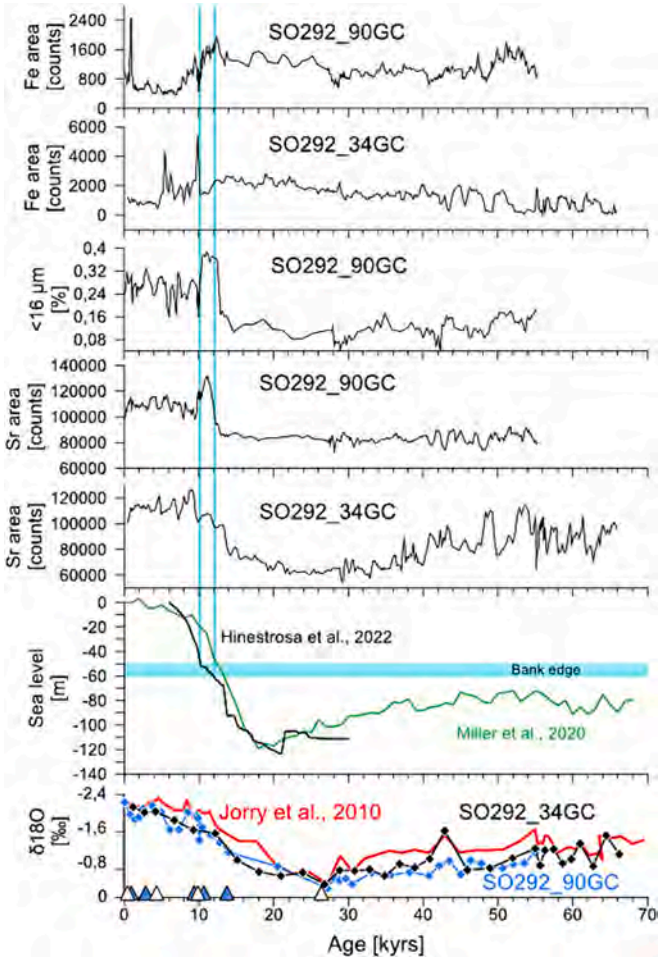

Fig. 15. The off-bank shedding pattern at the southern flank of Tregrosse bank is compared with the sea-level curves as presented in Hinestrosa et al. (2022) and Miller et al. (2020). Shallow-water export from the bank had a peak during the flooding of this bank edge when it was positioned in <20 m of water depth, i.e. in the optimal window for shallow-water carbonate production (blue rectangle). In the lower part of the figure the comparison of the oxygen isotope variations in cores SO292_34GC and SO292_90GC with the data presented by Jorry et al. (2010) for the northwestern Coral Sea. Triangles indicate age tie points based on radiocarbon dating (compare Table 1). (For interpretation of the references to colour in this figure legend, the reader is referred to the web version of this article.)

similarities with the main processes that destabilize carbonate platforms elsewhere (see introduction). Beyond this, for the first time, we show that the three processes slope erosion, slope destabilization, and submarine rockfalls act independently and in parallel to drive the dismantling of the windward flank of Tregrosse Bank (Fig. 16).

Erosion through sediment cascading from the inner platform acts in areas where the platform edge is deepest (segment 4), and where there is a pathway connecting the inner platform to the platform slope. The sedimentary record of the submarine fan indicates that this process is mostly active during sea-level falls, although megaripples and ripples at the floor of the feeder channels attest to active currents flowing at the present time.

The slopes lining areas with shallower edges and with less or more focused sediment export flows are characterized by submarine rockfalls. The resulting MTCs contain ridges and blocks indicating a collapsing platform edge or upper slope source. Slope over steepening, due to aggradation of the bank edge, could be a result of the combination of low sediment export from the platform interior, and the winnowing of sediment at the lower slope through bottom currents. Both processes would act in parallel by reducing the buttressing effect of sediment accumulated at the distal slope and toe of slope, as proposed by Lehrmann et al. (2020). The resulting slope instability in addition may be promoted by the differential rheological behavior of the underlying strata, i.e. stronger compaction in contrast to the rigid flank deposits, as described by Frost and Kerans (2009) and Nooitgedacht et al. (2018b).

6. Conclusions

The isolated mesophotic carbonate platform Tregrosse Bank is currently in a state of partial dismantling through slope instability and slope erosion. Two disconnected systems of submarine rockfalls and MTCs characterize the flanks of the platforms. Instability of the upper and middle slope results in blocks fields and MTCs lining the toe of the slopes of the bank. The triggering factors include the over-steepening of the bank margin due to low sediment input from the shallow platform areas and sediment winnowing at the toe of the slope by bottom currents. Further, seafloor instabilities in deeper parts of the slope are the consequence of deeper-rooted submarine landslides, probably along a lithological heterogeneity several hundreds of meters below the seafloor. Our data imply that lower and upper slope instabilities are disconnected. Slope erosion in the form of gullies and submarine valleys located in slope areas where the bank edge is submerged several 10s of meters allow a pathway of shallow-water sediment export. Reconstruction of the seismic morphology is an approach widely used for the interpretation of carbonate platform morphological evolution in subsurface data. A correct interpretation of features, however, needs modern counterparts to sharpen concepts. In this context, the modern Tregrosse Bank serves as an analog for many similar settings in the subsurface, assisting in the interpretation of platform evolution by demonstrating the complexity and relationship between carbonate platform slope dismantling processes. We regard the independency of the slope dismantling processes as key to better understand disintegration of partially drowned carbonate platforms.

CRediT authorship contribution statement

Sebastian Lindhorst: Writing – original draft, Methodology, Investigation, Funding acquisition, Formal analysis, Conceptualization. **Carola Hincke:** Visualization, Methodology, Formal analysis. **Jan Oliver Eisermann:** Writing – original draft, Visualization, Investigation, Data curation. **Or M. Bialik:** Writing – original draft, Investigation, Formal analysis. **Alex Petrovic:** Writing – original draft, Investigation, Formal analysis. **Jesus Reolid:** Writing – original draft, Investigation, Formal analysis. **Robin J. Beaman:** Writing – original draft, Methodology, Investigation, Formal analysis. **Jody M. Webster:** Writing – original draft, Investigation, Formal analysis. **Thomas Lüdmann:** Writing – original draft, Methodology, Investigation, Funding acquisition, Formal analysis. **Christian Hübscher:** Writing – original draft, Investigation, Funding acquisition, Formal analysis.

Declaration of competing interest

The authors declare the following financial interests/personal relationships which may be considered as potential competing interests: Christian Betzler reports financial support and equipment, drugs, or supplies were provided by Bundesministerium für Bildung und Forschung. If there are other authors, they declare that they have no known competing financial interests or personal relationships that could have appeared to influence the work reported in this paper.

Data availability

The link to the SO292 multibeam data is available at https://www2.bsh.de/daten/DOD/Bathymetrie/Suedpazifik/so292.htm. The sedimentological data for cores described herein are provided in the

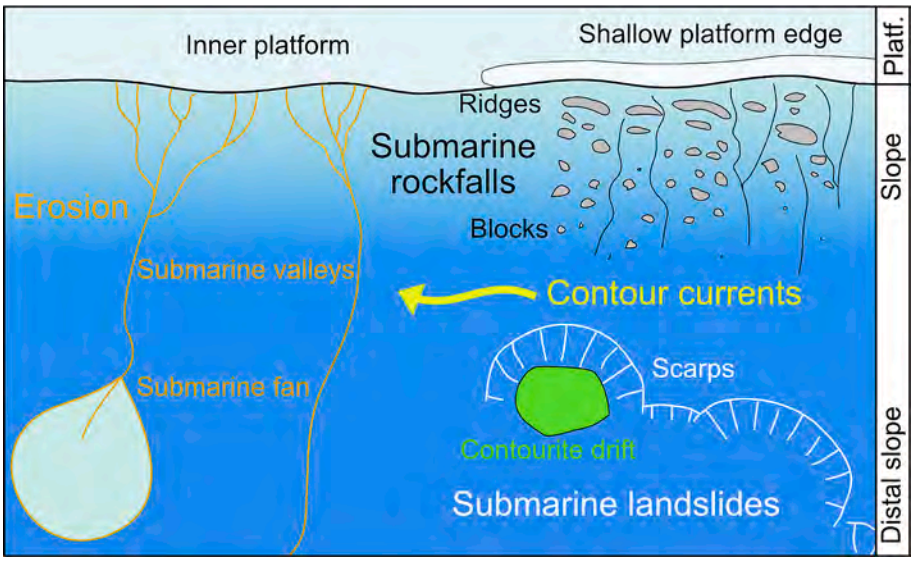

Fig. 16. Map view showing the main processes and products of the dismantling of the southern flank of Tregrosse Bank. See text for discussion. The figure is not to scale.

Supplements 2 and 3.

Parasound data are available from the data depository PANGAEA under doi.pangaea.de/https://doi.org/10.1594/PANGAEA.969088.

Acknowledgements

We thank the officers and crew of RV *Sonne* for the unlimited support during Cruise SO292. The shipboard scientific party and the technicians with their assistance provided the solid fundament that helped to acquire the data used in this study; a big thank to all of them. The Schmidt Ocean Institute is thanked for the RV *Falkor* multibeam data acquired during cruises FK200429 and FK200802. The Australian Hydrographic Office is thanked for the bathymetry lidar data collected over the Queensland Plateau banks and reefs, and AusTides predicted tides software for the study area. Victoria Strehse and Linus Budke are thanked for the postprocessing of the raw multibeam data, and Jutta Richarz for the laboratory work. This research used data acquired at the XRF Core Scanner Lab at the MARUM – Center for Marine Environmental Sciences, University of Bremen, Germany. We thank Parks Australia for the research permit for Cruise SO292 (permit EPBC 2022/9168). This study was funded through grant 03G0292A – ICECARB from the Federal Ministry of Education and Research to CB. JR thanks the Spanish Ministry of Science and Innovation (MCIN) for funding through the Ramón y Cajal Project RYC2021-034362-I (MCIN/AEI/10.13039/501100011033 and NextGenerationEU/PRTR. The constructive reviews by John Counts and two anonymous reviewers as well as the comments by the journal editor helped us to sharpen the manuscript.

Appendix A. Supplementary data

Supplementary data to this article can be found online at https://doi.org/10.1016/j.margeo.2024.107361.

References

Adams, E.W., Kenter, J.A.M., 2014. So different, yet so similar: Comparing and contrasting siliciclastic and carbonate slopes. In: Verwer, K., Playton, T.E., Harris, P. M. (Eds.), Deposits, Architecture, and Controls of Carbonate Margin, Slope and Basinal Settings. SEPM Special Publication. SEPM Society for Sedimentary Geology, Tulsa, pp. 14–25. https://doi.org/10.2110/sepmsp.105.14.

Andresen, N., Reijmer, J.J.G., Droxler, A.W., 2003. Timing and distribution of calciturbidites around a deeply submerged carbonate platform in a seismically active setting (Pedro Bank, Northern Nicaragua rise, Caribbean Sea). Int. J. Earth Sci. 92, 573–592. https://doi.org/10.1007/s00531-003-0340-0.

Beaman, R.J., 2010. High-resolution depth model for the Great Barrier Reef and Coral Sea - 100 m. Geosci Australia, Canberra. https://doi.org/10.26186/5e2f8bb629d07.

Betzler, C., Hübscher, C., Lindhorst, S., Lüdmann, T., Hincke, C., Beaman, R.J., Webster, J.M., 2024. Seismic stratigraphic and sedimentary record of a partial carbonate platform drowning, Queensland Plateau, north-East Australia. Mar. Geol. 470, 107255 https://doi.org/10.1016/j.margeo.2024.107255.

Bialik, O.M., Betzler, C., Braga, J.C., Reijmer, J.J.G., Reolid, J., Lindhorst, S., 2024. Changes in mesophotic carbonate-platform export across the end of the last glacial cycle (Saya de Malha Bank, western Indian Ocean). Depositional Rec. https://doi.org/10.1002/dep2.299.

Blott, S.J., Pye, K., 2001. GRADISTAT: a grain size distribution and statistics package for the analysis of unconsolidated sediments. Earth Surf. Process. Landf. 26, 1237–1248.

Borgomano, J.R.F., 2000. The Upper cretaceous Carbonates of the Gargano-Murge Region, Southern Italy: a model of Platform-To-Basin transition. AAPG Bull. 84, 1561–1588. https://doi.org/10.1306/8626BF01-173B-11D7-8645000102C1865D.

Bosellini, A., Neri, C., Luciani, V., 1993. Platform margin collapses and sequence stratigraphic organization of carbonate slopes: cretaceous? Eocene, Gargano Promontory, southern Italy. Terra Nova 5, 282–297. https://doi.org/10.1111/j.1365–3121.1993.tb00259.

Busson, J., Teles, V., Mulder, T., Joseph, P., Guy, N., Bouziat, A., Danquigny, C., Poli, E., Borgomano, J., 2021. Submarine landslides on a carbonate platform slope: forward numerical modelling of mechanical stratigraphy and scenarios of failure precondition. Landslides 18, 595–618.

Ceccarelli, D.M., McKinnon, A.D., Andréfouet, S., Allain, V., Young, J., Gledhill, D.C., Flynn, A., Bax, N.J., Beaman, R., Borsa, P., Brinkman, R., Bustamante, R.H., Campbell, R., Cappo, M., Cravatte, S., D'Agata, S., Dichmont, C.M., Dunstan, P.K., Dupouy, C., Edgar, G., Farman, R., Furnas, M., Garrigue, C., Hutton, T., Kulbicki, M., Letourneur, Y., Lindsay, D., Menkes, C., Mouillot, D., Parravicini, V., Payri, C., Pelletier, B., Richer de Forges, B., Ridgway, K., Rodier, M., Samadi, S., Schoeman, D., Skewes, T., Swearer, S., Vigliola, L., Wantiez, L., Williams, A., Williams, A., Richardson, A.J., 2013. The Coral Sea. Adv. Mar. Biol. 66, 213–290.

Counts, J.W., Jorry, S.J., Leroux, E., Miramontes, E., Jouet, G., 2018. Sedimentation adjacent to atolls and volcano-cored carbonate platforms in the Mozambique Channel (SW Indian Ocean). Mar. Geol. 404, 41–59. https://doi.org/10.1016/j.margeo.2018.07.003.

Counts, J.W., Jorry, S.J., Vazquez Riveiros, N., Jouet, G., Giraudeau, J., Cheron, S., Boissier, A., Miramontes, E., 2019. A late Quaternary record of highstand shedding from an isolated carbonate platform (Juan de Nova, southern Indian Ocean). Depositional Rec. 5, 540–557.

Counts, J.W., Jorry, S.J., Vazquez-Riveiros, N., Amy, L.A., Dennielou, E., Jouet, G., 2021. Sedimentology and distribution of late quaternary calciturbidites and calcidebrites in the Mozambique Channel (Southwest Indian Ocean). Facies 67, 17. https://doi.org/10.1007/s10347-021-00624-1.

Davies, P.J., Symonds, P.A., Feary, D.A., Pigram, C.J., 1989. The evolution of the carbonate platforms of Northeast Australia. In: Crevello, P. D., Wilson, J. L., Sarg, J. F., Read, J. F. (Eds.), Controls on carbonate platform and basin development. Soc. econ. Paleont. Mineral. Spec. Publ. 44, 233–258.

Davies, P.J., McKenzie, J.A., Palmer-Julson, A., et al., 1991. Proc. Proj., Init. Repts, Ocean Drill, p. 133.

De Deckker, P., Munday, C.I., Brocks, J., O'Loingsigh, T., Allison, G.E., Hope, J., Norman, M., Stuut, J.-B.W., Tapper, N.J., van der Kaars, S., 2014. Characterisation of the major dust storm that traversed over eastern Australia in September 2009; a multidisciplinary approach. Aeolian Res. 15, 133–149.

Droxler, A.W., Schlager, W., 1985. Glacial versus interglacial sedimentation rates and turbidite frequency in the Bahamas. Geology 13, 799–802.

Eberli, G.P., Anselmetti, F.S., Betzler, C., Van Konijnenburg, J.H., Bernoulli, D., 2005. Carbonate platform to basin transitions on seismic data and in outcrops: Great Bahama Bank and the Maiella Platform margin, Italy. AAPG Mem. 81, 207–250.

Etienne, S., Le Roy, P., Tournadour, E., Roest, W.R., Jorry, S., Collot, J., Patriat, M., Largeau, M.A., Roger, J., Clerc, C., Dechnick, B., Sanborn, K.L., Lepareur, F., Horowitz, J., Webster, J.M., Gaillot, A., 2021. Large-scale margin collapses along a partly drowned, isolated carbonate platform (Lansdowne Bank, SW Pacific Ocean). Mar. Geol. 436, 106477.

Fitzsimmons, K.E., Cohen, T.J., Hesse, P.P., Jansen, J., Nanson, G.C., May, J.-H., Barrows, T.T., Haberlah, D., Hilgers, A., Kelly, T., Larsen, J., Lomax, J., Treble, P., 2013. Late Quaternary palaeoenvironmental change in the Australian drylands. Quat. Sci. Rev. 74, 78–96. doi.org/10.1016/j.quascirev.2012.09.007.

Folk, R.L., Ward, W.C., 1957. Brazos River bar: a study in the significance of grain size parameters. J. Sediment. Res. 27, 3–26.

Frost, E.L., Kerans, C., 2009. Platform-margin Trajectory as a Control on Syndepositional Fracture patterns, Canning Basin, Western Australia. J. Sediment. Res. 79, 44–55. https://doi.org/10.2110/jsr.2009.014.

Ganachaud, A., Kessler, W., Wijffels, S., Ridgway, K., Cai, W., Holbrook, N., Bowen, M., Sutton, P., Qiu, B., Timmermann, A., Roemmich, D., Sprintall, J., Cravatte, S., Gourdeau, L., Aung, T., 2007. Southwest Pacific Ocean Circulation and climate Experiment (SPICE) - part I. Scientific background. CLIVAR Publication Series 111. NOAA/OAR special Rep 46. www.pmel.noaa.gov/pubs/PDF/gana3070/gana3070.pdf.

Ginsburg, R.N., Harris, P.M., Eberli, G.P., Swart, P.K., 1991. The growth potential of a bypass margin, Great Bahama Bank. J. Sediment. Petrol. 61, 976–987. https://doi.org/10.1306/D426781B-2B26-11D7-8648000102C1865D.

Glaser, K.S., Droxler, A.W., 1993. Controls and development of late Quaternary Periplatform Carbonate stratigraphy in Walton Basin (Northeastern Nicaragua rise, Caribbean Sea). Paleoceanography 8, 243–274. https://doi.org/10.1029/92PA02876.

Heaton, T., Köhler, P., Butzin, M., Bard, E., Reimer, R., Austin, W., Bronk Ramsey, C., Grootes, P., Hughen, K., Kromer, B., Reimer, P., Adkins, J., Burke, A., Cook, M., Olsen, J., Skinner, L., 2020. Marine20 - the marine radiocarbon age calibration curve (0–55,000 cal BP). Radiocarbon 62. https://doi.org/10.1017/RDC.2020.68.

Hinestrosa, G., Webster, J.M., Beaman, R.J., 2022. New constraints on the postglacial shallow-water carbonate accumulation in the Great Barrier Reef. Sci. Rep. 12, 924. https://doi.org/10.1038/s41598-021-04586-w.

Jo, A., Eberli, G.P., Grasmueck, M., 2015. Margin collapse and slope failure along southwestern Great Bahama Bank. Sediment. Geol. 317, 43–52. https://doi.org/10.1016/j.sedgeo.2014.09.004.

Jorry, S.J., Droxler, A.W., Mallarino, G., Dickens, G.R., Bentley, S.J., Beaufort, L., Peterson, L.C., Opdyke, B.N., 2008. Bundled turbidite deposition in the central Pandora Trough (Gulf of Papua) since last Glacial Maximum: linking sediment nature and accumulation to sea level fluctuations at millennial timescale. J. Geophys. Res. 113, F01S19 https://doi.org/10.1029/2006JF000649.

Jorry, S.J., Droxler, A.W., Francis, J.M., 2010. Deepwater carbonate deposition in response to re-flooding of carbonate bank and atoll-tops at glacial terminations. Quat. Sci. Rev. 29, 2010–2026. https://doi.org/10.1016/j.quascirev.2010.04.016.

Jorry, S.J., Jouet, G., Edinger, E.N., Toucanne, S., Counts, J.W., Miramontes, E., Courgeon, S., Riveiros, N.V., Le Roy, P., Camoin, G.F., 2020. From platform top to adjacent deep sea: New source-to-sink insights into carbonate sediment production and transfer in the SW Indian Ocean (Glorieuses archipelago). Mar. Geol. 423, 106144 https://doi.org/10.1016/j.margeo.2020.106144.

Kessler, W.S., Cravatte, S., 2013. Mean circulation of the Coral Sea. J. Geophys. Res. Oceans 118, 6385–6410.

Knapp, K.R., Kruk, M.C., Levinson, D.H., Diamond, H.J., Neumann, C.J., 2010. The International best Track Archive for climate Stewardship (IBTrACS). Bull. Am. Meteorol. Soc. 91, 363–376.

Kunkelova, T., Jung, S.J.A., de Leau, E.S., Odling, N., Thomas, A.L., Betzler, C., Eberli, G. P., Alvarez-Zarikian, C.A., Alonso-García, M., Bialik, O.M., Blättler, C.L., Guo, J.A., Haffen, S., Horozal, S., Mee, A.L.H., Inoue, M., Jovane, L., Lanci, L., Laya, J.C., Lüdmann, T., Bejugam, N.N., Nakakuni, M., Niino, K., Petruny, L.M., Pratiwi, S.D., Reijmer, J.J.G., Reolid, J., Slagle, A.L., Sloss, C.R., Su, X., Swart, P.K., Wright, J.D., Yao, Z., Young, J.R., Lindhorst, S., Stainbank, S., Rueggeberg, A., Spezzaferri, S., Carrasqueira, I., Yu, S., Kroon, D., 2018. A two million year record of low-latitude aridity linked to continental weathering from the Maldives. Prog Earth Planet Sci 5, 86. https://doi.org/10.1186/s40645-018-0238-x.

Le Goff, J., Slootman, A., Mulder, T., Cavailhes, T., Ducassou, E., Hanquiez, V., Jaballah, J., Reijmer, J.J.G., 2020. On the architecture of intra-formational mass-transport deposits: Insights from the carbonate slopes of Great Bahama Bank and the Apulian Carbonate Platform. Mar. Geol. 427, 106205 https://doi.org/10.1016/j.margeo.2020.106205.

Lehrmann, D.J., Minzoni, M., Enos, P., Kelleher, C., Stepchinski, L., Li, X., Payne, J.L., Yu, M., 2020. Giant sector-collapse structures (scalloped margins) of the Yangtze Platform and Great Bank of Guizhou, China: Implications for genesis of collapsed carbonate platform margin systems. Sedimentology 67, 3167–3198.

Lindhorst, S., Betzler, C., Kroon, D., 2019. Wind variability over the northern Indian Ocean during the past 4 million years – Insights from coarse aeolian dust (IODP exp. 359, site U1467, Maldives). Palaeogeogr. Palaeoclimatol. Palaeoecol. 536, 109371.

Liu, J., Liu, K., Salles, T., Li, C., 2022. Factors controlling carbonate slope failures: Insight from stratigraphic forward modelling. Earth Sci. Rev. 232, 104108. doi.org/10.1016/j.earscirev.2022.104108.

Micallef, A., Paull, C.K., Saadatkhah, N., Bialik, O., 2021. The Role of Fluid Seepage in the Erosion of Mesozoic Carbonate Escarpments. J. Geophys. Res. Earth 126, e2021JF006387.

Miller, K.G., Browning, J.V., Schmelz, W.J., Kopp, R.E., Mountain, G.S., Wright, J.D., 2020. Cenozoic Sea-level and cryospheric evolution from deep-sea geochemical and continental margin records. Science. Advances 6, eaaz1346.

Morsilli, M., Rusciadelli, G., Bosellini, A., 2002. Large-scale gravity-driven structures: control on margin architecture and related deposits of a cretaceous carbonate platform Montagna della Maiella. Central Apennines, Italy: Bollettino della Società Geologica Italiana 1, 619–628.

Morsilli, M., Hairabian, A., Borgomano, J., Nardon, S., Adams, E., Bracco Gartner, G., 2021. A Journey along the Gargano Promontory (Southern Italy): The Late Jurassic to Eocene Apulia Carbonate Platform Evolution. In. In: Field guides to exceptionally exposed carbonate outcrops. International Association of Sedimentologists, pp. 395–480.

Mulder, T., Ducassou, E., Eberli, G.P., Hanquiez, V., Gonthier, E., Kindler, P., Principaud, M., Fournier, F., Leonide, P., Billeaud, I., Marsset, B., Reijmer, J.J.G., Bondu, C., Joussiaume, R., Pakiades, M., 2012. New insights into the morphology and sedimentary processes along the western slope of Great Bahama Bank. Geology 40, 603–606. https://doi.org/10.1130/G32972.1.

Mulder, T., Ducassou, E., Gillet, H., Hanquiez, V., Principaud, M., Chabaud, L., Eberli, G. P., Kindler, P., Billeaud, I., Gonthier, E., Fournier, F., Léonide, P., Borgomano, J., 2014. First Discovery of Channel–Levee Complexes In A Modern Deep-Water Carbonate Slope Environment. J. Sediment. Res. 84, 1139–1146.

Mullins, H.T., Hine, A.C., 1989. Scalloped bank margins: beginning of the end for carbonate platforms? Geology 17, 30–33.

Mutter, J.C., 1977. The Queensland Plateau. Bur. Min. Resour., Geol. Geophys. Bull 179, 1–55.

Nooitgedacht, C.W., Kleipool, L.M., Andeweg, B., Reolid, J., Betzler, C., Lindhorst, S., Reijmer, J.J.G., 2018a. New insights in the development of syn-depositional fractures in rimmed flat-topped carbonate platforms, Neogene carbonate complexes, Sorbas Basin. SE Spain. Basin Res. 30, 596–612. https://doi.org/10.1111/bre.12239.

Nooitgedacht, C.W., Kleipool, L.M., Andeweg, B., Reolid, J., Betzler, C., Lindhorst, S., Reijmer, J.J.G., 2018b. New insights in the development of syn-depositional fractures in rimmed flat-topped carbonate platforms, Neogene carbonate complexes, Sorbas Basin. SE Spain. Basin Res. 30, 596–612. https://doi.org/10.1111/bre.12239.

Orme, G.R., 1977. The Coral Sea Plateau - a major reef province. In. In: Jones, O.A., Endean, R. (Eds.), Biology and Geology of Coral Reefs. Academic Press, New York, pp. 267–306.

Petherick, L.M., McGowan, H.A., Kamber, B.S., 2009. Reconstructing transport pathways for late Quaternary dust from eastern Australia using the composition of trace elements of long traveled dist. Geomorphology 105, 67–79.

Petrovic, A., Lüdmann, T., Afifi, A.M., Saitz, Y., Betzler, C., Vahrenkamp, V., 2023. Fragmentation, rafting, and drowning of a carbonate platform margin in a rift-basin setting. Geology 51, 242–246.

Principaud, M., Mulder, T., Gillet, H., Borgomano, J., 2015. Large-scale carbonate submarine mass-wasting along the northwestern slope of the Great Bahama Bank (Bahamas): Morphology, architecture, and mechanisms. Sediment. Geol. 317, 27–42. https://doi.org/10.1016/j.sedgeo.2014.10.008.

Puga-Bernabéu, A., Webster, J.M., Beaman, R.J., Guilbaud, V., 2011. Morphology and controls on the evolution of a mixed carbonate–siliciclastic submarine canyon system, Great Barrier Reef margin, North-Eastern Australia. Mar. Geol. 289, 100–116. https://doi.org/10.1016/j.margeo.2011.09.013.

Puga-Bernabéu, A., Beaman, R.J., Webster, J.M., Thomas, A.L., Jacobsen, G., 2017. Gloria Knolls Slide: a prominent submarine landslide complex on the Great Barrier Reef margin of North-Eastern Australia. Mar. Geol. 385, 68–83. https://doi.org/10.1016/j.margeo.2016.12.008.

Puga-Bernabéu, A., López-Cabrera, J., Webster, J.M., Beaman, R.J., 2022. Submarine landslide morphometrics and slope failure dynamics along a mixed carbonate-siliciclastic margin, North-Eastern Australia. Geomorphology 403, 108179.

Reolid, J., Bialik, O.M., Lindhorst, S., Eisermann, J.O., Petrovic, A., Hincke, C., Beaman, R.J., Webster, J.M., Betzler, C., 2024. A New Type of *Halimeda* Bioherm on the Queensland Plateau. Coral reefs, NE Australia. doi.org/10.1007/s00338-024-02500-0.

Rivera-Araya, M., Rowe, C., Ulm, S., Bird, M.I., 2022. A 33,000-year paleohydrological record from Sanamere Lagoon, north-eastern tropical savannas of Australia. Quat. Res. 1–16. https://doi.org/10.1017/qua.2022.59, 2022.

Sælen, G., Spalluto, L., Jensen, N.B., Grunnaleite, I., Sande, A.J.H., Svendsen, P.O.E., Osso, G., Paoli, N., Talbot, M.R., 2024. Diagenesis of carbonate density-flow deposits controlled by differential uplift of platform segments: examples from the cretaceous of the Gargano Promontory, Italy. J. Sediment. Res. 94, 1–36.

Schlager, W., 2005. Carbonate sedimentology and sequence stratigraphy. Concepts Sediment. Paleont. 8, 200.

Schlager, W., Reijmer, J.J.G., Droxler, A., 1994. Highstand shedding of carbonate platforms. J. Sediment. Res. 64, 270–281. https://doi.org/10.1306/D4267FAA-2B26-11D7-8648000102C1865D.

Siwabessy, J., Spinoccia, M., 2022. Processed EM710 Acoustic Backscatter, Sidescan and Swath Bathymetry Data acquired during R/V Falkor expedition FK200802 (2020). IEDA. https://doi.org/10.26022/IEDA/330880.

Spence, G.H., Tucker, M.E., 1997. Genesis of limestone megabreccias and their significance in carbonate sequence stratigraphic models: a review. Sediment. Geol. 112, 163–193. https://doi.org/10.1016/S0037-0738(97)00036-5.

Struckmeyer, H.I.M., Symonds, P.A., 1997. Tectonostratigraphic evolution of the Townsville Basin, Townsville Trough, offshore northeastern Australia. Aust. J. Earth Sci. 44, 799–817.

Stuiver, M., Reimer, P.J., 1993. CALIB rev. 8. Radiocarbon 35, 215–230.

Tournadour, E., Mulder, T., Borgomano, J., Hanquiez, V., Ducassou, E., Gillet, H., 2015. Origin and architecture of a Mass Transport complex on the northwest slope of Little Bahama Bank (Bahamas): Relations between off-bank transport, bottom current

sedimentation and submarine landslides. Sediment. Geol. 317, 9–26. https://doi.org/10.1016/j.sedgeo.2014.10.003.

Tournadour, E., Mulder, T., Borgomano, J., Gillet, H., Chabaud, L., Ducassou, E., Hanquiez, V., Etienne, S., 2017. Submarine canyon morphologies and evolution in modern carbonate settings: the northern slope of Little Bahama Bank. Bahamas. Mar. Geol. 391, 76–97. https://doi.org/10.1016/j.margeo.2017.07.014.

Webster, J.M., Beaman, R.J., Puga-Bernabéu, A., Ludman, D., Renema, W., Wust, R.A.J., George, N.P.J., Reimer, P.J., Jacobsen, G.E., Moss, P., 2012. Late Pleistocene history of turbidite sedimentation in a submarine canyon off the northern Great Barrier Reef. Australia. Palaeogeogr. Palaeoclimatol. Palaeoecol. 331–332, 75–89. https://doi.org/10.1016/j.palaeo.2012.02.034.

Webster, J.M., George, N.P.J., Beaman, R.J., Hill, J., Puga-Bernabéu, Á., Hinestrosa, G., Abbey, E.A., Daniell, J.J., 2016. Submarine landslides on the Great Barrier Reef shelf edge and upper slope: a mechanism for generating tsunamis on the north-east Australian coast? Mar. Geol. 371, 120–129.

Williams, M., Cook, E., van der Kaars, S., Barrows, T., Shulmeister, J., Kershaw, P., 2009. Glacial and deglacial climatic patterns in Australia and surrounding regions from 35 000 to 10 000 years ago reconstructed from terrestrial and near-shore proxy data. Quat. Sci. Rev. 28, 2398–2419.

Wilson, P.A., Roberts, H.H., 1995. Density cascading; off-shelf sediment transport, evidence and implications, Bahama Banks. J. Sediment. Res. 65, 45–56. https://doi.org/10.1306/D426801D-2B26-11D7-8648000102C1865D.

Wunsch, M., Betzler, C., Lindhorst, S., Lüdmann, T., Eberli, G.P., 2017. Sedimentary dynamics along carbonate slopes (Bahamas archipelago). Sedimentology 64, 631–657. https://doi.org/10.1111/sed.12317.